J. Fluid Mech. (1991), *vol.* 227, *pp.* 71–106
Printed in Great Britain

The influence of stratification on secondary instability in free shear layers

By G. P. KLAASSEN[1] AND W. R. PELTIER[2]
[1] Department of Earth and Atmospheric Science, York University, North York, Ontario
Canada M3J 1P3
[2] Department of Physics, University of Toronto, Toronto, Ontario Canada M5S 1A7

(Received 30 December 1989 and in revised form 20 July 1990)

We analyse the stability of horizontally periodic, two-dimensional, finite-amplitude Kelvin–Helmholtz billows with respect to infinitesimal three-dimensional perturbations having the same streamwise wavelength for several different levels of the initial density stratification. A complete analysis of the energy budget for this class of secondary instabilities establishes that the contribution to their growth from shear conversion of the basic-state kinetic energy is relatively insensitive to the strength of the stratification over the range of values considered, suggesting that dynamical shear instability constitutes the basic underlying mechanism. Indeed, during the initial stages of their growth, secondary instabilities derive their energy predominantly from shear conversion. However, for initial Richardson numbers between 0.065 and 0.13, the primary source of kinetic energy for secondary instabilities at the time the parent wave climaxes is in fact the conversion of potential energy by convective overturning in the cores of the individual billows. A comparison between the secondary instability properties of unstratified Kelvin–Helmholtz billows and Stuart vortices is made, as the latter have often been assumed to provide an adequate approximation to the former. Our analyses suggest that the Stuart vortex model has several shortcomings in this regard.

1. Introduction

The origin of three-dimensional motions and turbulence in free shear layers remains a subject of considerable interest in the literature, having been reviewed recently by Ho & Huerre (1984) and Bayly, Orszag & Herbert (1988) for the homogeneous case, and by Thorpe (1987) for the density-stratified case. Experimental investigations by Browand (1966), Freymuth (1966), Thorpe (1968, 1971, 1973), Miksad (1972), Browand & Winant (1973), Brown & Roshko (1974), Koop & Browand (1979), Breidenthal (1981) and others focused on the emergence of Kelvin–Helmholtz (KH) vortices in the shear layer. To varying degrees, each of these investigators noted the subsequent development of large-amplitude three-dimensional motions and eventually turbulence. The nonlinear nature of the initially dominant two-dimensional vortices has been addressed in theoretical studies by Maslowe (1973), Patnaik, Sherman & Corcos (1976), Peltier, Hallé & Clark (1978), Davis & Peltier (1979) and Klaassen & Peltier (1985*a*). Further experimental analyses by Jimenez, Cogollos & Bernal (1985), Thorpe (1985), Bernal & Roshko (1986), Lasheras, Cho & Maxworthy (1986) and Lasheras & Choi (1988) have established that three-dimensional motions are intimately associated with the development of streamwise vorticity.

Various theoretical studies have focused on the origin of three-dimensional motions in unstratified free shear layers. Pierrehumbert & Widnall (1982) considered the stability of steady inviscid Stuart vortices, while Nagata & Busse (1983) have analysed the stability of steady nonlinear vortices in a viscous inclined layer. Corcos & Lin (1984) and Metcalfe *et al.* (1987) have performed initial-value simulations of the development of three-dimensional motions in temporally evolving viscous free shear layers. Corcos & Lin attributed the onset of three-dimensional motions in the vortex core to the translative instability of Pierrehumbert & Widnall (1982), and Lin & Corcos (1984) presented a simple model of the generation of streamwise vorticity under the influence of plane strain to elucidate the development of three-dimensional motions in the braids. There seems to be some uncertainty as to whether three-dimensionality originates in the spanwise vortex cores or in the braids. Metcalfe *et al.* (1987) assert that they were unable to determine whether the streamwise vortex ribs appearing in their unstratified shear layer simulations were generated through a flow transition originating in the vortex cores (such as the translative instability of Pierrehumbert & Widnall 1982) or whether some other instability mechanism had come into play.

The origin of three-dimensional motions in the stratified free shear layer problem has also been considered theoretically. Davis & Peltier (1979) argued that wave-induced overturning of the stratification in the vortex core should lead to the onset of shear-aligned longitudinal convection rolls. This hypothesis was subsequently confirmed through the theoretical analyses of Klaassen & Peltier (1985*b, c*) for a single value of the initial Richardson number ($Ri = 0.07$), and later through the tilted-tube experiments of Thorpe (1985).

In this paper we shall consider in detail the influence that density stratification has on the stability of two-dimensional Kelvin–Helmholtz waves. The spectrum of infinitesimal perturbations against which the stability of these waves will be tested is fully three-dimensional but restricted to the same streamwise period as the basic nonlinear wave. Klaassen (1991) has examined the impact of varying stratification upon subharmonic instabilities (including those that induce vortex merging, a process discussed at length in Klaassen & Peltier 1989 for a single level of stratification).

2. Two-dimensional finite-amplitude disturbances in free shear layers

In order to obtain the basic states required for the stability analyses, finite-amplitude Kelvin–Helmholtz billows were simulated with an an elastic time-dependent two-dimensional finite-difference model (for a description of the model see Peltier *et al.* 1978). The profiles of velocity, $\boldsymbol{u} = (u_x, u_z)$, and potential temperature, θ, that determine the initial stratified parallel flow are

$$u_x(x,z,t=0) = u_0 \tanh\left(\frac{z-\frac{1}{2}H}{h}\right), \tag{2.1}$$

$$u_z(x,z,t=0) = 0, \tag{2.2}$$

$$\theta(x,z,t=0) = \Theta + \theta_0 \tanh\left(\frac{z-\frac{1}{2}H}{h}\right), \tag{2.3}$$

in which $2u_0$ is the velocity difference across the shear layer, $2h$ is the depth of the shear layer, H is the vertical domain height for the numerical model, Θ is the potential temperature of the hydrostatic isentropic background state, and $2\theta_0$ is the potential temperature difference across the interface. There are three non-dimensional parameters relevant to this problem; namely, the Reynolds number $Re = v_0 h/\nu$, the bulk Richardson number $Ri = g\theta_0 h/\Theta u_0^2$ (which is the initial value of the minimum gradient Richardson number for the layer) and the Prandtl number $Pr = \nu/\kappa$. The parameters g, ν and κ are respectively the acceleration due to gravity, the kinematic viscosity, and the thermal diffusivity. Note that we have chosen h as the lengthscale, u_0 as the velocity scale, and θ_0 as the scale for potential temperature fluctuations. For the purposes of this study we shall fix the Reynolds number to the value $Re = 300$, the Prandtl number to $Pr = 1$, and investigate the influence of the Richardson number Ri over the range $0 \leqslant Ri \leqslant 0.16$. Patnaik *et al.* (1976) have previously simulated the evolution of nonlinear Kelvin–Helmholtz waves over a similar range of Ri (for a somewhat lower Reynolds number, $Re = 100$), but did not consider their stability against three-dimensional perturbations.

Periodic boundary conditions are enforced in the model so that the shear layer evolves in time only. In the present study the horizontal domain length L of the nonlinear model is set equal to 14 (in units of h), approximating the wavelength of the most unstable Kelvin–Helmholtz mode of the parallel flow according to linear theory. Thus vortex merging cannot occur. The model simulations were initiated with a disturbance corresponding to the most unstable eigenfunctions of the parallel flow defined by (2.1)–(2.3). The initial non-dimensional kinetic energy of this disturbance (see equation (2.4)) was set to the value $K = 2\times 10^{-3}$, which is slightly smaller than the critical value of $K \approx 10^{-2}$ corresponding to the onset of nonlinear effects as determined by Klaassen & Peltier (1989). This initialization scheme ensures that minimal mean flow diffusion occurs before nonlinear wave growth begins. A spatial resolution equal to 14/128 (in units of h) was employed in the numerical model.

If $(\tilde{u}_x, \tilde{u}_z)$ represents the instantaneous non-dimensional velocity vector of the nonlinear KH wave, then the wave kinetic energy per unit horizontal area is given by

$$K = \frac{1}{2L}\int_0^L \int_0^H \bar{\rho}[(\tilde{u}_x - \bar{u}_x)^2 + \tilde{u}_z^2]\,\mathrm{d}x\,\mathrm{d}z, \tag{2.4}$$

where the instantaneous mean horizontal velocity

$$\bar{u}_x = \frac{1}{L}\int_0^L \tilde{u}_x\,\mathrm{d}x \tag{2.5}$$

and $\bar{\rho}(z)$ is the non-dimensional density profile of the isentropic hydrostatic background state. The evolution of the wave kinetic energy K is shown in figure 1 for KH billows possessing several bulk Richardson numbers in the range $0 \leqslant Ri \leqslant 0.16$. It is evident from this figure that the maximum KH wave amplitude is limited by the presence of strong stable stratification in the parent parallel flow and that the time at which maximum K is achieved is delayed significantly by increased stratification. These characteristics are consistent with the expectation that the wave must perform work against the gravitational potential in order to grow.

Figure 1 also shows that the KH wave does not enter a steady state after its kinetic energy saturates. Instead, the wave kinetic energy begins to oscillate, a phenomenon which was reported earlier by Davis & Peltier (1979) for $Re = 500$, $Pr = 1$ and $Ri = 0.07$. By performing a full energy budget analysis, Klaassen & Peltier (1985*a*) were

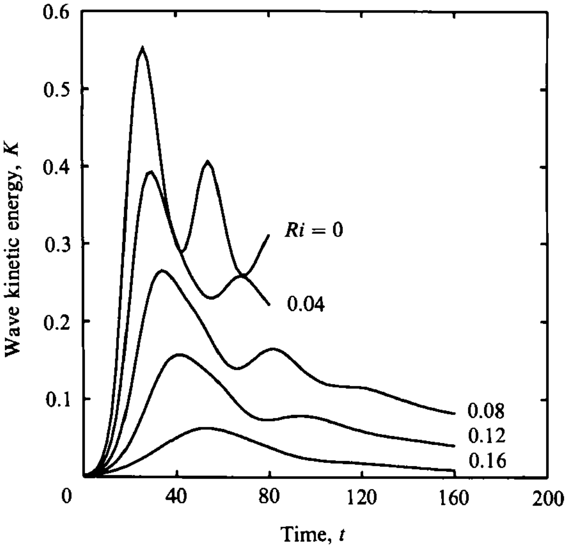

FIGURE 1. The effect of the bulk Richardson number on the evolution of wave kinetic energy (K), for nonlinear Kelvin–Helmholtz billows with Reynolds number $Re = 300$ and Prandtl number $Pr = 1$. The value of the Richardson number Ri is shown on each plot.

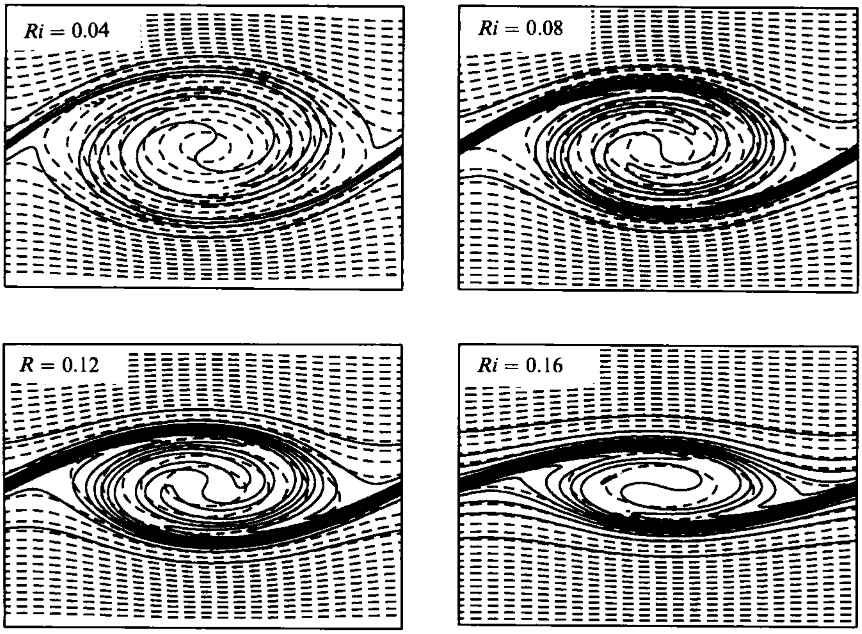

FIGURE 2. Stream function (dashed contours) and potential temperature field (solid contours) for stratified Kelvin–Helmholtz billows at various Richardson numbers Ri and $Re = 300$, $Pr = 1$. The waves are shown at the times of maximum kinetic energy, which are $t = 26$ ($Ri = 0$), 30 ($Ri = 0.04$), 34 ($Ri = 0.08$), 42 ($Ri = 0.12$) and 52 ($Ri = 0.16$). Contour intervals are the same for each wave. The horizontal period is $14h$ and the domain height is $10h$.

able to show that these oscillations were associated with an exchange of energy between the wave and the mean flow which involved a nutation of the KH vortex core. The data shown here indicate that as the Richardson number increases, the amplitude of the oscillations decreases and their period increases. This behaviour is

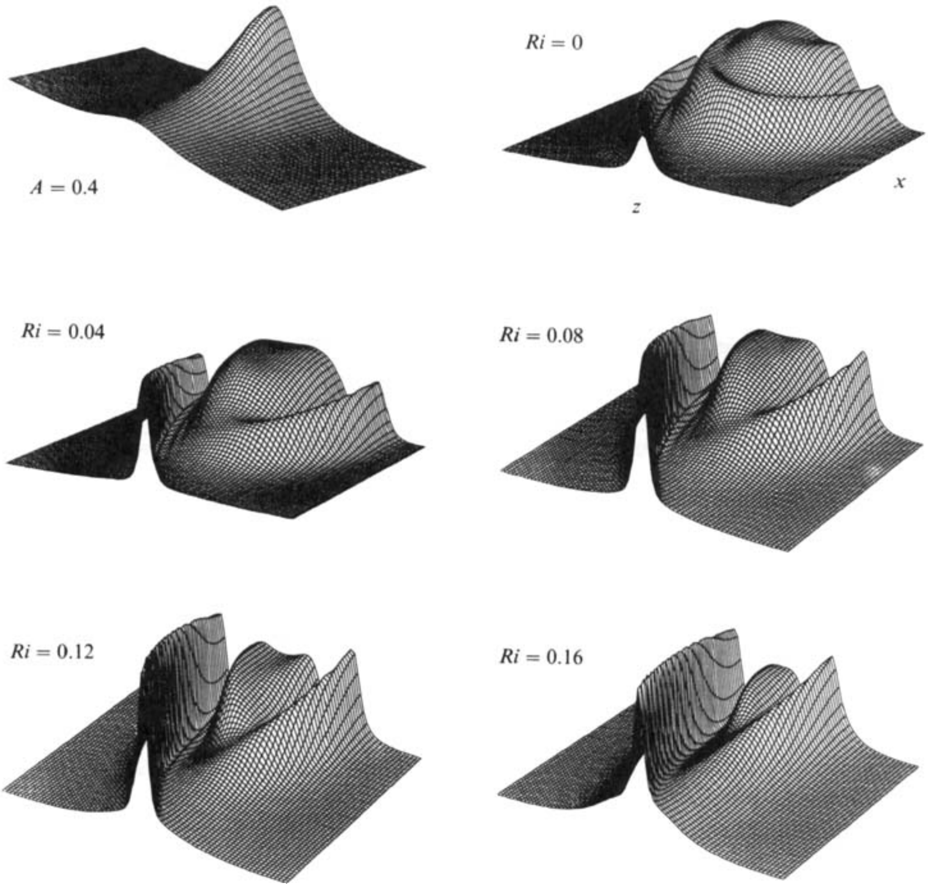

FIGURE 3. Surface plots of the vorticity field for Kelvin–Helmholtz billows with $Re = 300$, $Pr = 1$ and various values of Ri. Only the first half of the horizontal period is shown with the line of sight directed toward the leftmost stagnation point. The fields are shown at the times of maximum wave kinetic energy, which are given in figure 2. The vorticity field of an unstratified Stuart vortex of amplitude $A = 0.4$ is also shown for comparison purposes.

consistent with the expectation that stable stratification should inhibit the exchange of energy with the mean flow through the reduction of the wave's vertical velocity field which accompanies the conversion of kinetic into potential energy. As shall be discussed in what follows, the variability of KH waves has important implications for the stability analyses.

Figures 2 and 3 show the stream function, potential temperature and vorticity fields of nonlinear KH waves near the time of maximum wave kinetic energy for selected Richardson numbers. Note that at this particular time, the fluid in each of the vortex cores has been overturned, as will be clear upon inspection of the overlays of stream function and potential temperature presented in figure 2.

Figure 3 illustrates the vorticity maxima (ridges) associated with the braids, and the troughs associated with the entrainment of irrotational fluid into the vortex core. In the unstratified case $Ri = 0$, for which there is no baroclinic conversion, the vorticity is preferentially dissipated viscously in the braids due to the sharper gradients there. Thus, by the time the $Ri = 0$ wave achieves its maximum amplitude, the vorticity remaining in the core is substantially greater than that in the braids.

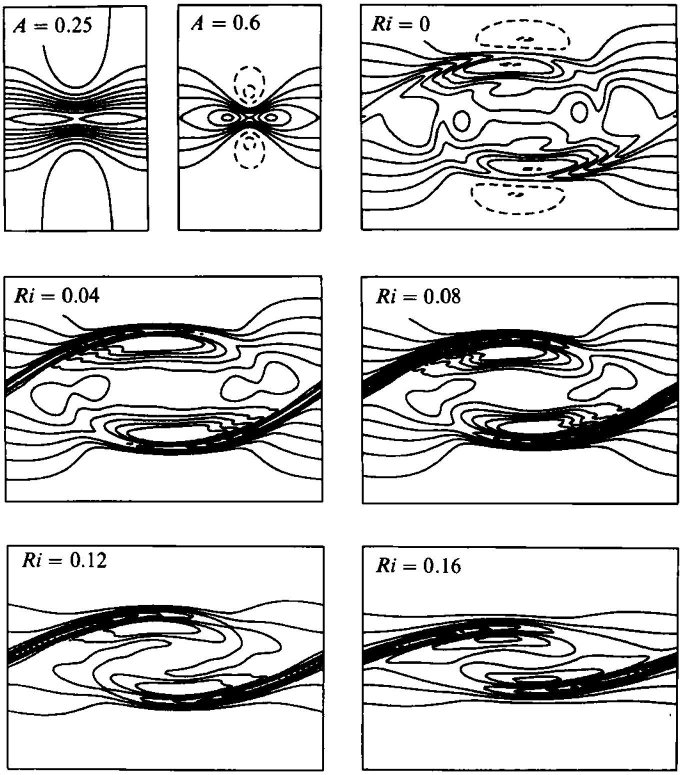

FIGURE 4. Shearing deformation fields ($\partial_z \tilde{u}_x + \partial_x \tilde{u}_z$) are shown for the same Kelvin–Helmholtz wave states as in figures 2 and 3. Contour intervals are δ for $Ri = 0, 0.04, 0.08$ and 2δ for $Ri = 0.12, 0.16$. Fields are also shown for Stuart vortices with $A = 0.25$ and 0.6.

In contrast, the braid vorticity exceeds that in the core for the maximum amplitude states with $Ri \geqslant 0.08$. This is due to the fact that vorticity is generated in the braids by baroclinic potential temperature gradients. Initially the vortex core is a site of baroclinic destruction of vorticity but, as the wave overturns, successive regions of baroclinic generation and destruction are introduced into the core. The net vorticity is almost conserved because the dissipation is weak, so the baroclinic terms in effect cause a net transfer of vorticity from the core to the braids (Klaassen & Peltier 1985*a*).

Figures 4 and 5 display the corresponding shearing and stretching deformation fields (defined in the figure captions) for the same maximum-amplitude KH wave states. These nonlinear fields, as we shall see, can play a significant role in the transfer of kinetic energy to secondary instabilities. The cat's eye of Kelvin can be readily identified in the shearing deformation field. Note that the closed contour region found in the upper and lower 'lids' of the eye represent local minima in shearing deformation, while the braids and the 'corners' of the cat's eye represent local maxima. As we shall see, these maxima at the lateral edges of the vortex core are sites where secondary instabilities extract energy from the basic KH wave.

Although the primary focus of this paper is on the stability of Kelvin–Helmholtz billows, for comparison purposes we also consider the stability of the family of steady two-dimensional solutions of the inviscid unstratified Euler equations reported by Stuart (1967). The stability of Stuart vortices has been addressed previously by

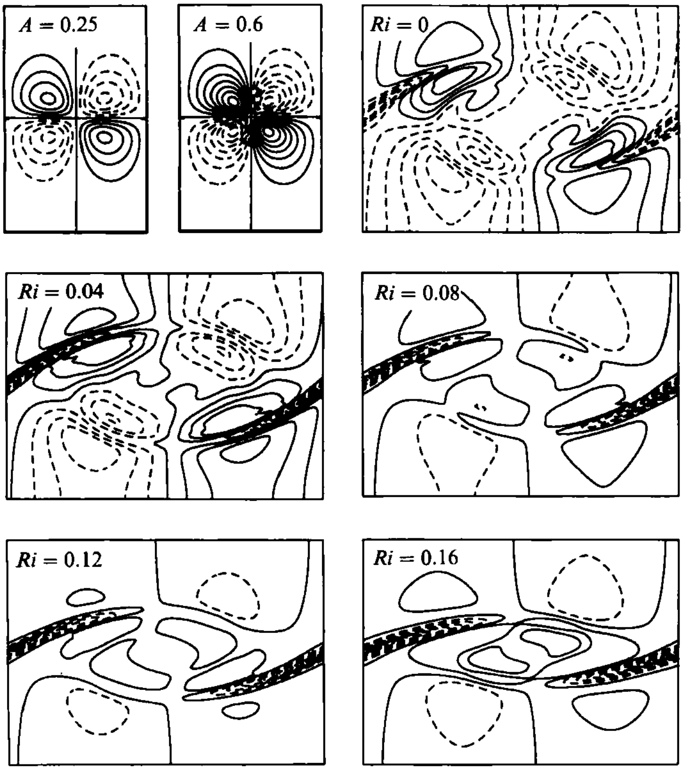

FIGURE 5. Stretching deformation fields $(\partial_x \bar{u}_x - \partial_z \bar{u}_z)$ are shown for the same Kelvin–Helmholtz wave states as in figures 2 and 3. Contour intervals are 0.1δ for $Ri = 0$, 0.04, 0.16 and 0.2δ for $Ri = 0.08$, 0.12. Fields are also shown for Stuart vortices with $A = 0.25$ and 0.6.

Pierrehumbert & Widnall (1982) and Klaassen & Peltier (1987, 1989). In dimensional form, the stream function of these Stuart vortices is given by

$$\psi = u_0 h \ln\left[\cosh\left(\frac{z-\frac{1}{2}H}{h}\right) + A\cos\left(\frac{x}{h}\right)\right], \tag{2.6}$$

while the vorticity has the analytic distribution

$$\zeta = \nabla^2\psi = \frac{u_0}{h}\left[\frac{1-A^2}{\cosh\left[(z-\frac{1}{2}H)/h\right] + A\cos(x/h)}\right]. \tag{2.7}$$

The parameter A represents the amplitude of the vortex, and varies from the value $A = 0$ corresponding to the parallel flow $u_x = u_0 \tanh\left[(z-\frac{1}{2})H/h\right]$, to the value $A = 1$, corresponding to a point vortex. The limitations of the Stuart vortex as a model of the nonlinear waves which are physically realizable in unstratified parallel flow have been discussed by Klaassen & Peltier (1989). Most importantly, the nature of real fluids leads to a non-stationary state which compresses the initial shear into thin braids that join the vortex cores and entrains fluid into the central vortex. As illustrated in figure 3, braid-like features are not found in Stuart vortices, although they do possess stagnation points similar to those found in KH billows. In what follows we shall discuss the extent to which the temporal and structural differences between Stuart vortices and Kelvin–Helmholtz billows affect their respective stability characteristics.

3. The method of stability analysis

As described more fully in Klaassen & Peltier (1985*b*), the problem of determining the stability of the nonlinear waves described above is formulated by expanding the total dimensional velocity and potential temperature fields as

$$u_i(x,y,z,t) = u_0\,\tilde{u}_i(x,z,t)[1-\delta_{i2}]+u_0\,u_i'(x,y,z,t), \tag{3.1}$$

$$\theta(x,y,z,t) = \Theta+\theta_0\,\tilde{\theta}(x,z,t)+\theta_0\,\theta'(x,y,z,t). \tag{3.2}$$

The y-axis ($i = 2$) is oriented in the spanwise direction, normal to the plane of the two-dimensional basic state. The quantities u_0, θ_0 and h are defined as representative scales of velocity, potential temperature and length associated with the initial basic state defined in (2.1)–(2.3). The two-dimensional fields denoted by $\tilde{u}_i$ and $\bar{\theta}$ represent either a nonlinear KH billow with non-dimensional wavenumber $\alpha = 0.45$ and streamwise wavelength $L = 2\pi/\alpha$, or a Stuart vortex with $\alpha = 1.0$ and $L = 2\pi$. For spatially bounded disturbances, Floquet theory dictates that the perturbations take the form

$$u_i'(x,y,z,t) = \hat{u}_i(x,z,t)\exp{[\mathrm{i}(bx+dy)]}, \tag{3.3}$$

$$\theta'(x,y,z,t) = \hat{\theta}(x,z,t)\exp{[\mathrm{i}(bx+dy)]}, \tag{3.4}$$

where $\hat{u}_i$ and $\hat{\theta}$ have a spatial period of L in the x-direction, and b and d are real. Note that in this study we shall focus on modes (u_i', θ') which have the same streamwise wavelength as the basic nonlinear wave (i.e. $b = 0$).

If the nonlinear states are steady, or vary sufficiently slowly compared to the perturbations, we may then write

$$\hat{u}_i(x,z,t) = u_i^\dagger(x,z)\,\mathrm{e}^{st}, \tag{3.5}$$

$$\hat{\theta}(x,z,t) = \theta^\dagger(x,z)\,\mathrm{e}^{st}, \tag{3.6}$$

with $s = \sigma+\mathrm{i}\omega$, thereby transforming the initial-value problem into an eigenvalue problem. The validity of this approximation must be subject to an *a posteriori* test. In particular, one is obliged to discard modes which possess growth rates $\sigma = Re\{s\}$ that do not satisfy the criterion

$$\sigma \gg |\sigma_{\mathrm{KH}}| = \left|\frac{1}{2K}\frac{\mathrm{d}K}{\mathrm{d}t}\right|, \tag{3.7}$$

where σ_{KH} is the rate of growth (or decay) of the nonlinear KH wave and K is defined by (2.4).

Substituting perturbation fields of the form (3.3)–(3.6) into the linearized Boussinesq equations yields the following set of stability equations:

$$su_x^\dagger+\tilde{u}_x(\partial_x+\mathrm{i}b)u_x^\dagger+\tilde{u}_z\,\partial_z\,u_x^\dagger+(\partial_x\,\tilde{u}_x)\,u_x^\dagger+(\partial_z\,\tilde{u}_x)\,u_z^\dagger = -(\partial_x+\mathrm{i}b)\,p^\dagger+\frac{1}{Re}\mathrm{L}_2\,u_x^\dagger, \tag{3.8}$$

$$su_y^\dagger+\tilde{u}_x(\partial_x+\mathrm{i}b)\,u_y^\dagger+\tilde{u}_z\,\partial_z\,u_y^\dagger = -\mathrm{i}dp^\dagger+\frac{1}{Re}\mathrm{L}_2\,u_y^\dagger, \tag{3.9}$$

$$su_z^\dagger+\tilde{u}_x(\partial_x+\mathrm{i}b)\,u_z^\dagger+\tilde{u}_z\,\partial_z\,u_z^\dagger+(\partial_x\,\tilde{u}_z)\,u_x^\dagger+(\partial_z\,\tilde{u}_z)\,u_z^\dagger = -\partial_z\,p^\dagger+Ri\,\theta^\dagger+\frac{1}{Re}\mathrm{L}_2\,u_z^\dagger, \tag{3.10}$$

$$s\theta^\dagger+\tilde{u}_x(\partial_x+\mathrm{i}b)\,\theta^\dagger+\tilde{u}_z\,\partial_z\,\theta^\dagger+(\partial_x\,\tilde{\theta})\,u_x^\dagger+(\partial_x\,\tilde{\theta})u_x^\dagger = \frac{1}{Re\,Pr}\mathrm{L}_2\,\theta^\dagger, \tag{3.11}$$

$$(\partial_x+\mathrm{i}b)\,u_x^\dagger+\mathrm{i}du_x^\dagger+\partial_z\,u_z^\dagger = 0, \tag{3.12}$$

$$\mathrm{L}_2p^\dagger = Ri\,\partial_z\,\theta^\dagger-2[(\partial_x\,\tilde{u}_x)(\partial_x+\mathrm{i}b)\,u_x^\dagger+(\partial_z\,\tilde{u}_z)\,\partial_z\,u_z^\dagger+(\partial_x\,\tilde{u}_z)\,\partial_z\,u_x^\dagger+(\partial_z\,\tilde{u}_z)(\partial_x+\mathrm{i}b)\,u_z^\dagger], \tag{3.13}$$

where the differential operator

$$\mathrm{L}_2 \equiv (\partial_x + \mathrm{i}b)^2 + \partial_z^2 - d^2. \tag{3.14}$$

The eigensystem (3.8)–(3.13) may be solved by expanding $u_x^\dagger, u_z^\dagger$, and $\theta^\dagger$ in a Galerkin basis as follows:

$$u_x^\dagger = \sum_{\lambda=-\infty}^{\infty} \sum_{\nu=0}^{\infty} a_{\lambda\nu} \mathrm{e}^{\mathrm{i}\lambda a x} \cos\left(\frac{\nu\pi z}{H}\right), \tag{3.15}$$

$$u_z^\dagger = \sum_{\lambda=-\infty}^{\infty} \sum_{\nu=1}^{\infty} b_{\lambda\nu} \mathrm{e}^{\mathrm{i}\lambda a x} \sin\left(\frac{\nu\pi z}{H}\right), \tag{3.16}$$

$$\theta^\dagger = \sum_{\lambda=-\infty}^{\infty} \sum_{\nu=1}^{\infty} c_{\lambda\nu} \mathrm{e}^{\mathrm{i}\lambda a x} \sin\left(\frac{\nu\pi z}{H}\right). \tag{3.17}$$

(Note that the pressure and spanwise velocity eigenfunctions are eliminated as discussed in Klaassen & Peltier 1985*b*.) Substituting these Galerkin representations into the stability equations (3.8)–(3.13) and computing the inner product of each equation with the complex conjugate of the appropriate basis function yields the following closed system of algebraic equations:

$$sa_{\kappa\mu} = \left[I^{(1)}_{\kappa\mu\lambda\nu} - \frac{A_{\lambda\nu}}{Re}\delta_{\kappa\lambda}\delta_{\mu\nu}\right] a_{\lambda\nu} + I^{(2)}_{\kappa\mu\lambda\nu} b_{\lambda\nu} + Ri\left[\frac{\mathrm{i}B_\kappa D_\mu}{A_{\kappa\mu}}\right]_{c\kappa\mu}, \tag{3.18}$$

$$sb_{\kappa\mu} = I^{(3)}_{\kappa\mu\lambda\nu} a_{\lambda\nu} + \left[I^{(4)}_{\kappa\mu\lambda\nu} - \frac{A_{\lambda\nu}}{Re}\delta_{\kappa\lambda}\delta_{\mu\nu}\right] b_{\lambda\nu} + Ri\left[\frac{1-D_\mu^2}{A_{\kappa\mu}}\right] c_{\kappa\mu}, \tag{3.19}$$

$$sc_{\kappa\mu} = I^{(5)}_{\kappa\mu\lambda\nu} a_{\lambda\nu} + I^{(6)}_{\kappa\mu\lambda\psi} b_{\lambda\nu} + \left[I^{(7)}_{\kappa\mu\lambda\nu} - \frac{A_{\lambda\nu}}{Re\,Pr}\delta_{\kappa\lambda}\delta_{\mu\nu}\right] c_{\lambda\nu}, \tag{3.20}$$

where
$$B_\lambda = \lambda a + b, \quad D_\nu = \frac{\psi\pi}{H}, \quad A_{\lambda\nu} = B_\lambda^2 + D_\nu^2 + d^2 \tag{3.21}$$

and summation over repeated indices is implied. The interaction matrices $I^{(n)}_{\kappa\mu\lambda\nu}$ consist of projections of the nonlinear two-dimensional fields onto the Galerkin basis, e.g.

$$I^{(6)}_{\kappa\mu\lambda\nu} = \frac{2}{LH}\int_0^L \int_0^H \exp\left[-\mathrm{i}(\kappa-\lambda)\,ax\right] \sin\left(\frac{\mu\pi z}{H}\right) \sin\left(\frac{\nu\pi z}{H}\right) \partial_z \tilde{\theta}\,\mathrm{d}x\,\mathrm{d}z. \tag{3.22}$$

Once the expansions (3.15)–(3.17) are truncated at some finite values of the indices, the eigensystem may be solved by standard matrix eigenvalue techniques. By solving (3.18)–(3.20) at various instants in the KH wave history we may identify the time of onset and duration of any secondary instability which the two-dimensional nonlinear wave might support, and obtain another means for assessing the physical importance of a particular mode of instability. Unless the growth rate is sustained for a sufficient length of time, the mode will not reach an amplitude large enough to significantly affect the evolution of the shear layer. Klaassen & Peltier (1985*b*) showed that the expected amplification factor for a particular mode over the interval $[T_2, T_1]$ could be satisfactorily estimated by

$$F = \exp\left[\int_{T_1}^{T_2} \sigma(t)\,\mathrm{d}t\right]. \tag{3.23}$$

The eigensystem defined by (3.8)–(3.13) possesses certain symmetries with respect to the spanwise wavenumber d and the Floquet exponent b. These may be summarized as follows:

I. If s is an eigenvalue at (b, d) with eigenvector $\{u_x^\dagger, u_y^\dagger, u_z^\dagger, \theta^\dagger, p^\dagger\}$ then s^* is also an eigenvalue at $(-b, d)$ with eigenvector $\{u_x^{\dagger *}, -u_y^{\dagger *}, u_z^{\dagger *}, \theta^{\dagger *}, p^{\dagger *}\}$.

II. The Floquet expansions (3.3)–(3.4) and (3.15)–(3.17), which are of the form

$$f'(x,y,z,t) = \left[\sum_{\lambda=-\infty}^{\infty} f_\lambda(z)\,\mathrm{e}^{\mathrm{i}\lambda a x}\right]\mathrm{e}^{\mathrm{i}(bx+dy)+st}, \tag{3.24}$$

are invariant under the transformation $b \rightarrow b + n\alpha$, where n is an integer.

III. Properties I and II immediately yield $s(\alpha - b, d) = s^*(b, d)$.

IV. If s is an eigenvalue at (b, d) with eigenvector $(u_x^\dagger, u_y^\dagger, u_z^\dagger, \theta^\dagger, p^\dagger)$ then s is also an eigenvalue at $(b, -d)$ with eigenvector $(u_x^\dagger, -u_y^\dagger, u_z^\dagger, \theta^\dagger, p^\dagger)$.

These properties permit us to restrict our search of the eigenspace to $0 \leqslant b \leqslant \frac{1}{2}\alpha$ and $d \geqslant 0$. In addition, properties I and III require the eigenvalues s to be real or to occur in complex-conjugate pairs when either $b = 0$ or $b = \frac{1}{2}\alpha/2$. The conjugate pairs of oscillatory modes may combine to form standing waves, with the nodes occurring at fixed locations along the spanwise axis. As in Klaassen & Peltier (1989), we employ a modified triangular truncation scheme of the form $2|\lambda + b/\alpha| + \nu \leqslant N$.

The stability results to be presented here have been thoroughly checked for convergence by examining the sensitivity of the growth rates to changes in the truncation parameter N and domain height H. The maximum truncation level obtainable was limited by the 4 million word memory of the Cray X-MP we employed, and corresponded to $N = 27$ for stratified waves and $N = 35$ in the case $Ri = 0$. Convergence tests were carried out using $N = 15$, 19, 23, 27 and 35. We also employed domain height values of $H = 8$, 10 and 14 to check the sensitivity of the results to the boundary conditions and to provide additional variability in resolution. The smooth dependence of the unstable eigenmodes on the spanwise wavenumber d permitted them to be grouped into branches based on continuity in growth rate and angular frequency. Eigenvectors of the fastest growing modes in each branch were also checked to ensure that there was no excessive small-scale structure indicative of resolution difficulties.

As shown by Klaassen & Peltier (1985*b*), the quantity

$$K'(x,z) = |u_x^\dagger|^2 + |u_y^\dagger|^2 + |u_z^\dagger|^2 \tag{3.25}$$

is directly related to the kinetic energy density of the unstable eigenmodes. One may construct a budget equation for K' by taking

$$(3.8) \times u_x^{\dagger *} + (3.8)^* \times u_x^\dagger + (3.9) \times u_y^{\dagger *} + (3.9)^* \times u_y^\dagger + (3.10) \times u_z^{\dagger *} + (3.10)^* \times u_z^\dagger,$$

where * denotes the complex conjugate. The result is

$$\begin{aligned} 2\sigma K' + \partial_x(\tilde{u}_x K') + \partial_z(\tilde{u}_z K') + 2(\partial_x \tilde{u}_z + \partial_z \tilde{u}_x)\,\mathrm{Re}\,\{u_x^{\dagger *} u_z^\dagger\} + (\partial_x \tilde{u}_x - \partial_z \tilde{u}_z)[|u_x^\dagger|^2 - |u_z^\dagger|^2] \\ = -\,2\partial_x\,[\mathrm{Re}\{u_x^{\dagger *} p^\dagger\}] - 2\partial_z[\mathrm{Re}\{u_z^{\dagger *} p^\dagger\}] + \frac{2}{Re}\{\mathrm{Re}\{u_x^{\dagger *}\mathrm{L}_2\, u_x^\dagger + u_y^{\dagger *}\mathrm{L}_2\, u_y^\dagger \\ + u_z^{\dagger *}\mathrm{L}_2\, u_z^\dagger\}] + 2Ri\,\mathrm{Re}\{u_z^{\dagger *}\theta^\dagger\}. \end{aligned} \tag{3.26}$$

As demonstrated in the context of a similar problem by Laprise & Peltier (1989), this quantity may be usefully averaged over the spatial domain of the nonlinear wave. For the present case, this gives the result:

$$\sigma\langle K' \rangle = \langle \mathscr{S}\mathscr{h} \rangle + \langle \mathscr{S}\mathscr{t} \rangle + \langle \mathscr{H} \rangle + \langle \mathscr{D} \rangle, \tag{3.27}$$

where we have introduced the integral operator $\langle\ \rangle$. The kinetic energy of the infinitesimal perturbation per unit horizontal area is given by

$$\langle K' \rangle = \frac{1}{L}\int_0^L \int_0^H K' \,\mathrm{d}x\,\mathrm{d}z \tag{3.28}$$

and the source/sink terms have the explicit forms:

$$\langle \mathscr{S}k \rangle = -\frac{1}{L}\int_0^L \int_0^H (\partial_x \tilde{u}_z + \partial_z \tilde{u}_x)\,\mathrm{Re}\{u_x^{\dagger *} u_z^{\dagger}\}\,\mathrm{d}x\,\mathrm{d}z, \tag{3.29}$$

$$\langle \mathscr{S}t \rangle = -\frac{1}{L}\int_0^L \int_0^H \tfrac{1}{2}(\partial_x \tilde{u}_x - \partial_z \tilde{u}_z)(|u_x^{\dagger}|^2 - |u_z^{\dagger}|^2)\,\mathrm{d}x\,\mathrm{d}z, \tag{3.30}$$

$$\langle \mathscr{H} \rangle = \frac{Ri}{L}\int_0^L \int_0^H \mathrm{Re}\{u_z^{\dagger *} \theta^{\dagger}\}\,\mathrm{d}x\,\mathrm{d}z, \tag{3.31}$$

$$\langle \mathscr{D} \rangle = \frac{1}{Re\,L}\int_0^L \int_0^H \mathrm{Re}\{u_x^{\dagger *} \mathrm{L}_2 u_x^{\dagger} + u_y^{\dagger *} \mathrm{L}_2 u_y^{\dagger} + u_z^{\dagger *} \mathrm{L}_2 u_z^{\dagger}\}\,\mathrm{d}x\,\mathrm{d}z. \tag{3.32}$$

The term $\langle \mathscr{S}k \rangle$ represents an interaction between the shearing deformation of the nonlinear wave and the Reynolds stress of the eigenmode, while $\langle \mathscr{S}t \rangle$ represents the interaction between the stretching deformation of the nonlinear wave and a quantity which measures the anisotropy in the (x, z)-components of the perturbation velocity. The $\langle \mathscr{H} \rangle$ the term represents the vertical flux of heat associated with the eigenmode, and $\langle \mathscr{D} \rangle$ the dissipation due to molecular viscosity.

If the source terms on the right-hand side of (3.27) are normalized by $\langle K' \rangle$, they then give absolute contributions to the growth rate. This form is useful for assessing the dependence of conversion terms on parameters such as Ri. Equation (3.27) was satisfied to better than 0.2% for the present calculations.

4. The stability of Kelvin–Helmholtz billows

In this section we will discuss the stability of Kelvin–Helmholtz billows with bulk Richardson numbers $Ri = 0$, 0.04, 0.08, 0.12 and 0.16. We shall consider only those unstable modes which possess the same streamwise wavelength as the basic nonlinear wave, i.e. those for which the Floquet parameter $b = 0$. (Other calculations not reported here indicate that the growth rates of most of the dominant instabilities do not vary appreciably with b.) Modes which have $d \neq 0$ are longitudinal and fully three-dimensional, while those with $d = 0$ are transverse and two-dimensional. For $b = 0$, it turns out that most of the unstable branches are clearly three-dimensional in nature, i.e. their maximum growth is achieved for non-zero spanwise wavenumber d, and this maximum value of σ is significantly larger than the value which obtains in the transverse limit.

Only those modes which exhibited a sufficient degree of convergence over the range of spanwise wavenumbers $0 \leqslant d \leqslant 5$ will be discussed in this paper. Unfortunately, this means that we must exclude from present consideration the non-oscillatory braid-distorting instability reported by Klaassen & Peltier (1989) for the case $Ri = 0.07$ and $d = 0$. This relatively short-lived mode was shown to consist of a dipole of spanwise vorticity with spatial dimensions on the order of the shear depth and was found to be confined to the vicinity of the KH wave stagnation points near

$z = \frac{1}{2}H$ and $x = 0, L$. Although this braid instability is adequately resolved for small spanwise wavenumbers near zero, it is not sufficiently well-resolved for values larger than $d \approx 0.5$. Specifically, the preferred spanwise wavenumber varies significantly within the range of truncation parameters available to us. The present calculations do suggest that this mode may exist over a wide range of spanwise wavenumbers and may in fact have maximum growth at some value of d different from zero. Thus it could conceivably play a role in the onset of three-dimensional small-scale disorder. However, the present results indicate that the maximum growth rates of these poorly resolved braid modes are at least a factor of two lower than those of the well-resolved fastest growing modes. It seems clear then that the well-resolved dominant modes are of primary interest in determining the onset of three-dimensional motions, and we shall therefore focus on them.

For KH waves with $Ri = 0.07$ (and various values of Re and Pr) Klaassen & Peltier (1985*b*, *c*) found that longitudinal secondary instabilities having $b = 0$ fall into several branches, each having a distinct frequency that varies only slowly with the spanwise wavenumber d. In particular, they were able to identify sequences of unstable branches that possessed similar eigenfunctions and had angular frequencies which *approximately* constituted the first few harmonics of a Fourier spectrum with period $2\pi/\Omega_P$, i.e. $\omega_n = \pm n\Omega_P$, where $n = 0, 1, 2, \ldots$. The modes with higher frequencies were generally found to have growth rates which were lower and were maintained over a shorter interval of time than those of the lower-frequency modes. For convenience we will refer to this sequence of unstable branches as the principal spectrum, and the branches themselves will be referred to by their individual frequencies, e.g. ω_0, ω_1, ω_2, etc.

The same sort of pattern emerges here for the other values of Ri. The principal modes arise in the vicinity of the entrainment troughs which are situated between the braids and the lateral edges of the vortex core. Their kinetic energy tends to be confined to a doubly connected region, specifically a cylindrical tube of elliptical cross-section which encircles the central vortex; little or no kinetic energy is present at the centre of the vortex. Their growth is engendered by velocity shear (i.e. deformation) and, in the case of stratified flow, by density inversions which develop as fluid is entrained into the central vortex. We have also been able to identify another class of modes which, during their entire lifetime, remain tightly confined to the central part of the vortex core. For many members of this class (including the most unstable modes), the kinetic energy is concentrated in a simply connected region which has a maximum or maxima near the vortex centre. The notation C_n will be employed for these 'central core' modes. Here the subscript n refers to the frequency of the mode, given by $\omega = \pm n\Omega_C$, $n = 0, 1, 2, \ldots$ In §5 we shall demonstrate that the C_0 mode is closely related to the translative instability of Stuart vortices reported by Pierrehumbert & Widnall (1982).

Since KH waves are not steady, the eigenvalues and eigenfunctions produced by the stability analysis will in general vary with time, and must be subjected to the validation test (3.7). In order to determine which secondary instabilities (with $b = 0$) are likely to be realized, one must examine their dependence on both the changing KH wave state and the spanwise wavenumber d. We shall therefore first consider the evolution of the dominant secondary instabilities of the principal and central core types for a few fixed wavenumbers. For each value of Ri considered here, the most unstable longitudinal modes achieve their largest rate of growth very near the time of maximum KH wave kinetic energy K (the climax state), so we shall then examine the stability properties of the climax KH wave states in more detail.

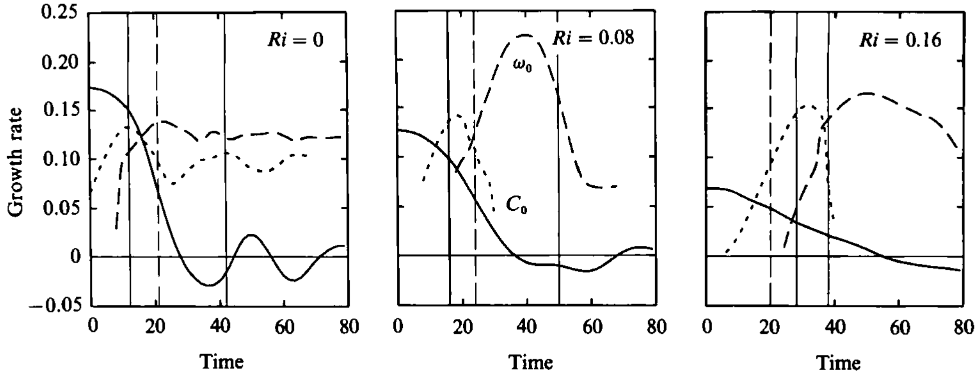

FIGURE 6. Effect of KH wave evolution on secondary instabilities for $Ri = 0$, 0.08, 0.16. In each case, the KH wave variations are represented by σ_{KH} (solid). For $Ri = 0$, the vertical lines are at $t = 12$, $21 (T_C)$, 42, while the secondary instabilities shown are ω_0 ($d = 1.8$, long dash) and C_0 ($d = 0.9$, short dash). For $Ri = 0.08$, the vertical lines are at $t = 16$, 24 (T_C), 50, while the secondary instabilities shown are ω_0 ($d = 3.0$, long dash), and C_0 ($d = 1.1$, short dash). For $Ri = 0.16$, the vertical lines are at $t = 20(T_C$ for $C_0)$, 28, 38, while secondary instabilities shown are ω_0 ($d = 2.8$, long dash), and C_0 ($d = 1.8$, short dash). $T_C = 30$ for ω_0.

4.1. *Temporal variation of secondary instabilities*

Figure 6 illustrates the effect that temporal variations in the background KH wave have on the growth rates of various secondary instabilities for $Ri = 0$, 0.08 and 0.16. The solid curves correspond to σ_{KH}, while the dashed curves are the growth rates of various unstable non-oscillatory modes for a fixed spanwise wavenumber. The dashed vertical lines correspond to the times T_C at which the secondary growth rates σ first exceed that of the primary (σ_{KH}) by a factor of two. T_C represents a reasonable estimate of the minimum time for which the criterion (3.7) is satisfied. (Klaassen & Peltier 1989 have demonstrated that the growth rates and eigenfunctions are remarkably accurate for two-dimensional vortex pairing instability even when $\sigma \sim \sigma_{\text{KH}}$.) For purposes of discussion, we have included results of the stability analysis for $t \leqslant T_C$. Strictly speaking, these data should not be used to draw quantitative conclusions regarding the behaviour of secondary instabilities at these early times. However, if we keep this limitation in mind, we shall see that results for $t \leqslant T_C$ provide some useful qualitative information.

Our analysis indicates that for $Ri = 0$, the central core instability C_0 onsets while the KH wave is itself growing rapidly, and its growth rate peaks for $t \approx 12 < T_C$. In §5 we shall present evidence that the C_0 mode is related to the instability of an elliptical vortex. When seen in this light, the early onset of C_0 is not surprising, and in fact provides support for the qualitative utility of the analysis for $t < T_C$. As the KH wave approaches maximum amplitude, the C_0 mode decays to a lower level of growth, and is superseded by the principal ω_0 mode. This latter mode attains maximum growth at $t \approx 22 > T_C$ and thereafter its growth rate varies little. Figure 7 demonstrates that throughout the lifetime of the C_0 mode, its kinetic energy remains confined to a simple maximum located at the centre of the vortex. In contrast, the largest values of ω_0 kinetic energy are found near the braid stagnation points and, at later times, along the side of braids which is adjacent to the entrainment troughs. At all stages of its development, the K' field of the ω_0 mode possesses a characteristic doubly connected shape.

Amplification factors $F(t_1, t_2)$ (based on (3.23)) which estimate the potential growth of various unstable modes over the interval (t_1, t_2) are presented in table 1. The

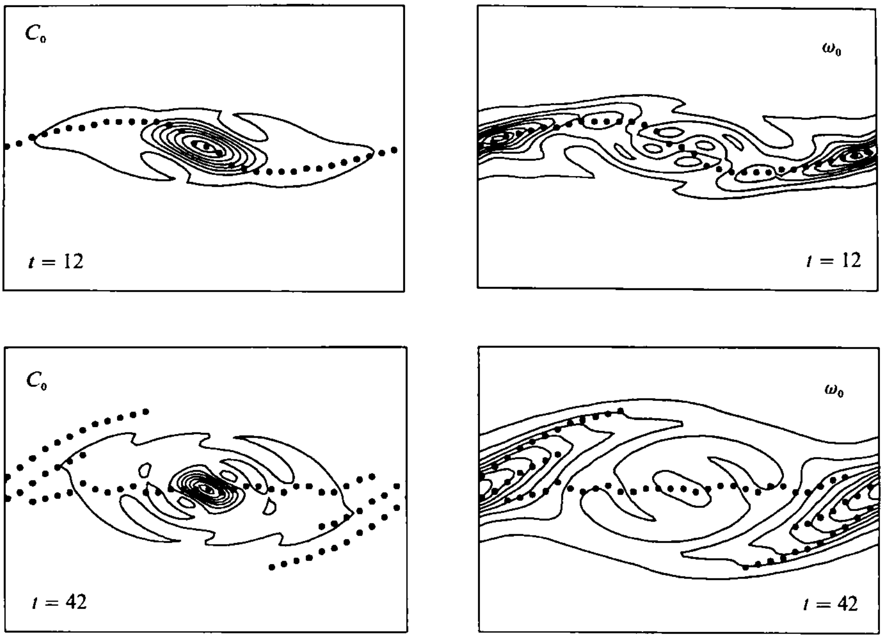

FIGURE 7. Kinetic energy correlations K' for the C_0 and ω_0 modes of the unstratified ($Ri = 0$) KH wave at $t = 12(d = 0.9)$, $42(d = 1.5)$. See figures 14 and 15 for $t = 26$ and further details.

Ri	Mode	T_C	$T(0, T_C)$	$F(T_C, T_C+30)$	$F(0, T_C+30)$
0	ω_0	21	4.4	45	200
0	C_0	24	15	17	260
0.08	ω_0	24	2.8	270	760
0.08	C_0	24	10	$\geqslant 2$	$\geqslant 20$
0.16	ω_0	30	1.3	72	94
0.16	C_0	20	1.9	$\geqslant 12$	$\geqslant 24$

TABLE 1. Amplification factors $F(T_1, T_2)$ (see (3.23)) for various secondary instabilities of KH waves. T_C is the first time for which $\sigma \geqslant 2\sigma_{KH}$.

factors $F(0, T_C)$ provide an estimate of potential amplification which may occur before the criterion (3.7) is satisfied and should therefore be considered only as qualitative estimates. The factors $F(T_C, T_C+30)$ provide quantitative values for the amplification experienced after the criterion is satisfied, and values in excess of ~ 50 should be considered significant. The values $F(0, T_C) = 4.4$ and 15 for ω_0 and C_0 respectively indicate that neither mode is likely to achieve an amplitude sufficient to significantly alter the primary KH flow before T_C. (If they did, the analysis would be inconclusive.) During the interval (T_C, T_C+30), the ω_0 mode grows by a factor of 45, while the C_0 mode only grows by a factor of 17. These values indicate that the principal ω_0 mode will lead to the development of nonlinear three-dimensional motions. The fate of the C_0 core mode is not as clear, although if the estimated growth rates for $t \leqslant T_C$ are assumed to be reasonable, the combined amplification of C_0 for the interval $(0, T_C+30)$ is comparable with that of the principal ω_0 mode. This suggests that the C_0 mode will also be realized for $Ri = 0$, and that it is likely to achieve an amplitude of order unity at roughly the same time as the ω_0 mode.

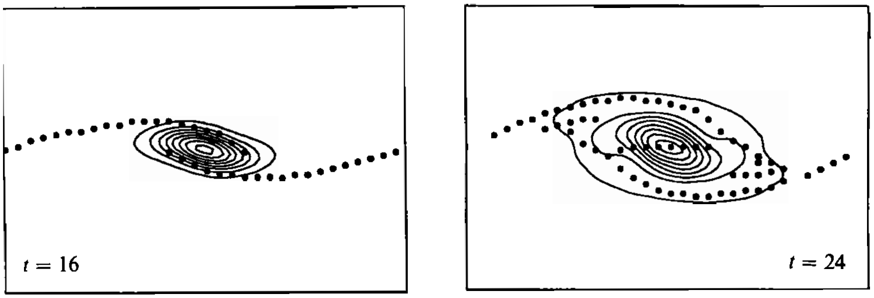

FIGURE 8. Kinetic energy correlations K' for the C_0 mode of the $Ri = 0.08$ KH wave at $t = 16$, 24 for $d = 1.2$.

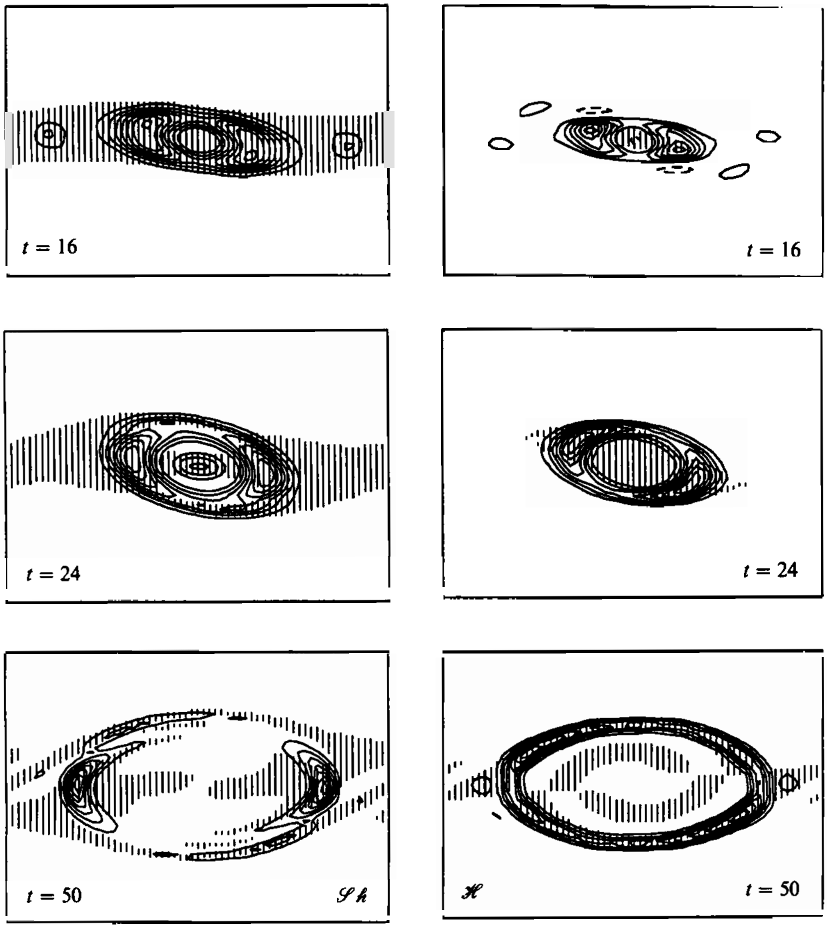

FIGURE 9. $\mathscr{S}\mathscr{h}$ and $\mathscr{H}$ conversions for the ω_0 mode of the $Ri = 0.08$ KH wave at $t = 16(d = 1.2)$, $24(d = 1.8)$, $50(d = 3.5)$. See figures 14 and 17 for an explanation of the shaded regions.

Figure 6 demonstrates that for $Ri = 0.08$ the C_0 central core mode also onsets before the principal ω_0 mode, during the period in which the KH wave is still growing rapidly. The maximum growth rates achieved by the C_0 mode at $Ri = 0.08$ are similar to those of the corresponding unstratified mode, although they occur somewhat later in the present case. However, as the KH wave approaches maximum amplitude, the

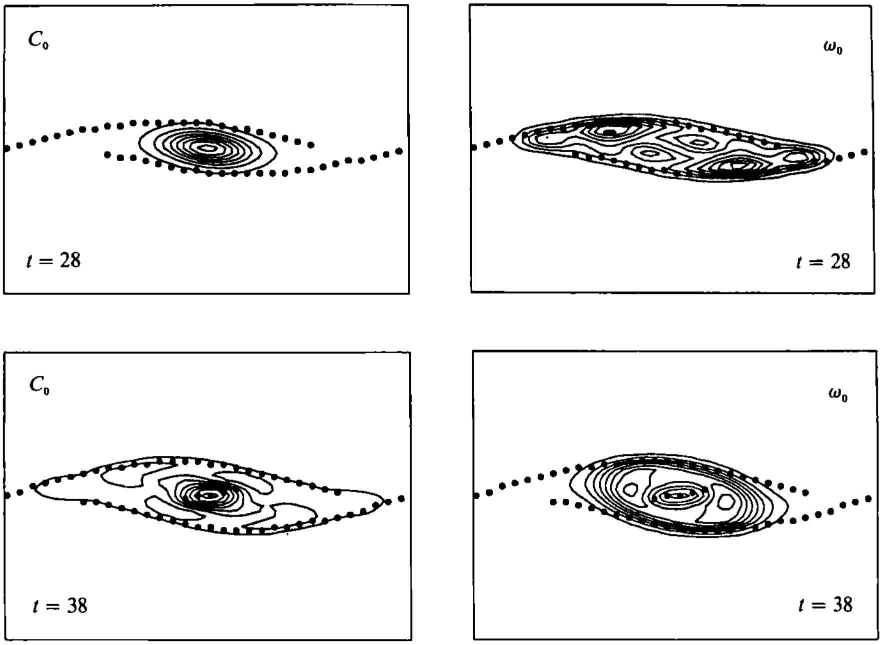

FIGURE 10. Kinetic energy correlations K' for the C_0 and ω_0 modes of the $Ri = 0.16$ KH wave at $t = 28$, 38, for $d = 2.0$. See figure 21 for $t = 52$.

growth rate of the C_0 mode decays to a very low level, while the growth rate of the ω_0 mode achieves much higher levels than its unstratified counterpart. The amplification factors for $Ri = 0.08$ presented in table 1 indicate that the C_0 mode is unlikely to experience significant growth. For this level of stratification, we therefore expect the three-dimensional motions introduced by the principal ω_0 mode to dominate over those of the central core mode C_0.

Figure 8 demonstrates that for $Ri = 0.08$, the kinetic energy of the C_0 mode remains confined to a simply connected region at the centre of the vortex. On the other hand, figure 9 clearly shows that the $\mathscr{S}k$ and $\mathscr{H}$ energy conversions of the principal ω_0 mode have a doubly connected structure even during the early stages ($t = 16$, 24) when the superadiabatic region itself is simply connected. Note that the $\mathscr{S}k$ conversion remains confined to the lateral edges of the vortex core, while $\mathscr{H}$ remains correlated with the primary superadiabatic region, even after a new superadiabatic region appears at the vortex centre as the wave overturns for a second time ($t = 50$).

The case of $Ri = 0.16$ is rather similar to the others we have considered in that the C_0 central core mode onsets first. However, the C_0 mode for $Ri = 0.16$ achieves $\sigma \geqslant 2\sigma_{\mathrm{KH}}$ at $T_C = 20$, much earlier than does the ω_0 mode (which has $T_C = 30$). The amplification factors presented in table 1 indicate that the C_0 mode is not likely to achieve significant amplitudes before ω_0, which is attributable to the rapid decay of the C_0 growth rate at $t \approx 38$. Thus we would expect the longer-lived principal ω_0 mode to be primarily responsible for the development of a secondary three-dimensional flow at $Ri = 0.16$. Note that in this case, most of the C_0 growth occurs during the period in which its growth rate is large compared to that of the primary wave, so that this information is of quantitative value. Figure 10 shows the kinetic energy correlations of the C_0 and ω_0 modes for $Ri = 0.16$ at $t = 28$, 38. The KH wave

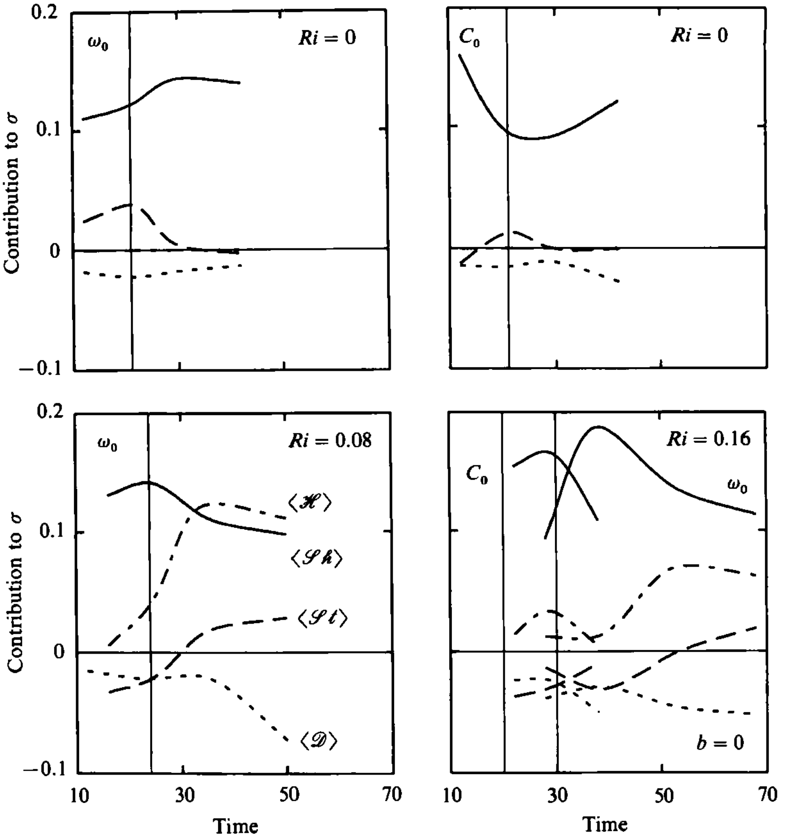

FIGURE 11. The effect of KH wave evolution on energy conversions for the ω_0 and C_0 modes of KH waves having $Ri = 0$, and 0.16 and the ω_0 mode of the $Ri = 0.08$ wave. The $Ri = 0.08$ C_0 mode conversions (not shown) are similar to those of the $Ri = 0.16$ case. [$\langle \mathscr{S}k \rangle$ solid]; [$\langle \mathscr{S}t \rangle$ long dash] [$\langle \mathscr{H} \rangle$ dash-dot] [$\langle \mathscr{D} \rangle$ short dash]. The conversion terms given in (3.29)–(3.32) are normalized by $\langle K' \rangle$, giving individual contributions to the growth rate σ.

first overturns at $t \approx 22$ and the resulting primary superadiabatic region retains its simply connected shape until $t \approx 40$. The C_0 mode exhibits a single maximum of K' at the vortex centre during this time whereas the strongest K' for ω_0 is concentrated at the lateral edges of the vortex core.

Figure 11 presents the contributions of the energy conversions to the growth rates of various modes. $\langle \mathscr{S}k \rangle$ conversion dominates over $\langle \mathscr{S}t \rangle$ conversion for both the C_0 and ω_0 modes in the unstratified case. For the C_0 modes of the stratified waves, the $\langle \mathscr{H} \rangle$ and $\langle \mathscr{S}t \rangle$ conversions remain small and their dominant source of energy throughout their lifetime is $\langle \mathscr{S}k \rangle$ conversion (the C_0 mode for $Ri = 0.08$ has not been shown since it is similar to $Ri = 0.16$). The sharp decrease in C_0 growth rates which occurs as the KH wave approaches the climax state is therefore due to a decrease in the efficiency of the $\langle \mathscr{S}k \rangle$ conversion.

Both the ω_0 modes for $Ri = 0.08$ and 0.16 initially derive their energy almost exclusively from $\langle \mathscr{S}k \rangle$ conversion. For $Ri = 0.16$, $\langle \mathscr{S}k \rangle$ conversion provides the major source of growth throughout its lifetime, although $\langle \mathscr{H} \rangle$ conversion partially offsets the decrease in $\langle \mathscr{S}k \rangle$ conversion as the amplitude of the KH wave increases. In the case of $Ri = 0.08$, the $\langle \mathscr{H} \rangle$ conversion surpasses the $\langle \mathscr{S}k \rangle$ extraction as the KH wave approaches maximum amplitude, demonstrating that the release of

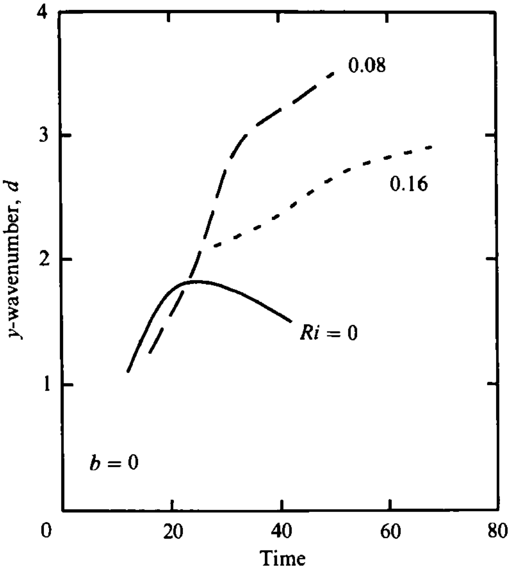

FIGURE 12. Effect of KH wave evolution on the preferred spanwise wavenumber d of the principal ω_0 modes of the $Ri = 0$, 0.08, and 0.16 KH waves.

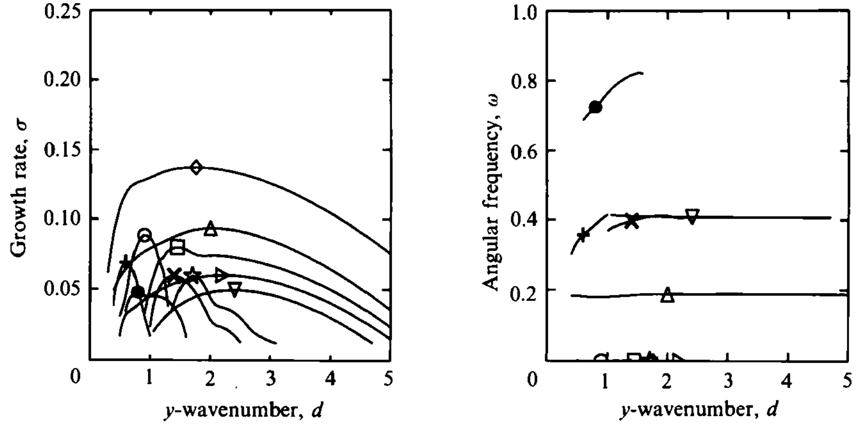

FIGURE 13. Growth rate σ and angular frequency ω vs. spanwise (y) wavenumber d for the maximum-amplitude state of a nonlinear KH wave with bulk Richardson number $Ri = 0$. (For $b = 0$). The symbols on each σ *vs.* d curve denote the fastest growing mode, and the same symbol is used to label the corresponding ω *vs.* d curve. Note that only the non-negative eigenfrequencies are shown.

potential energy through convection is responsible for the substantially larger growth rate relative to the $Ri = 0$ and 0.16 cases. The sharp decrease in the ω_0 growth rate for $Ri = 0.08$ seen for $t > 34$ is primarily due to an increase in the magnitude of the dissipation term $\langle \mathscr{D} \rangle$ as the vertical scale of the statically unstable region becomes increasingly smaller.

Figure 12 presents the evolution of the spanwise wavenumber of the most unstable principal ω_0 modes for $Ri = 0$, 0.08, and 0.16. It should be mentioned that these secondary instabilities have broad bandwidths, and so these values of d are not strongly preferred. However, the fastest growing spanwise wavenumbers are initially low and, for stratified flow, tend to become larger as the nonlinear KH wave evolves.

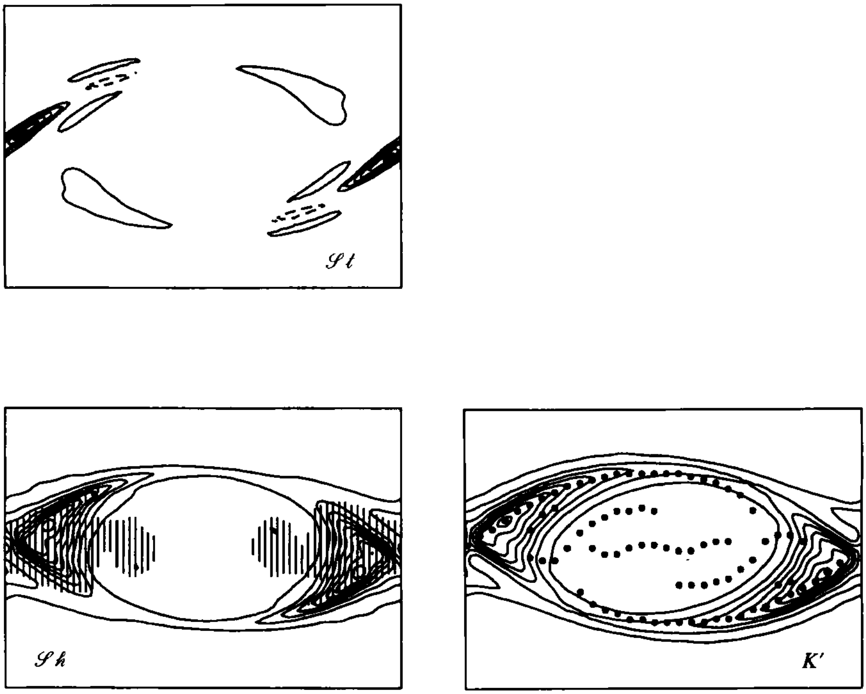

FIGURE 14. Eigenfunction correlations depicting the spatial dependence of the kinetic energy and the energy transfers for the most unstable ω_0 mode (labelled ◇ in figure 13) of the maximum-amplitude KH wave with $Ri = 0$. Here $t = 26$, $b = 0$, $d = 1.8$, $\sigma = 0.137$, $\omega = 0$. $\langle \mathscr{S}k \rangle = 0.145$, $\langle \mathscr{S}t \rangle = 0.012$, $\langle \mathscr{H} \rangle = 0$, $\langle \mathscr{D} \rangle = -0.020$ in units of $\langle K' \rangle$. The shearing conversion $\mathscr{S}k(x, z)$ and the stretching conversion $\mathscr{S}t(x, z)$ are given by the integrands in equations (3.29)–(3.30) respectively, while the perturbation kinetic energy density K' is given by (3.25). The vertical lines superimposed on the $\mathscr{S}k$ field represent the regions of the nonlinear KH wave where the shearing deformation exceeds 0.43 of its maximum value. This fraction was chosen so as to reveal the detailed structure of the deformation field on the wave core. The dots superimposed on the K' field mark the position of vertical line maxima in the vorticity field, which mark the location of the braids and the vorticity ridges in the core. The domain length and height are respectively 14 and 10 (in units of h).

These trends are understandable since the modes arise initially as a response to the deformation field of the large-scale primary vortex, and, as the nonlinear wave rolls up, the scale of the unstable region decreases. The preferred value of d for the C_0 modes is not shown in figure 12, but tends to remain within a factor of two of unity.

4.2. *Stability of the climax states*

The growth rates σ and corresponding angular frequencies ω of the unstable modes of the maximum-amplitude unstratified KH wave state have been plotted against the spanwise wavenumber in figure 13. The branches labelled ◇ ($\omega_0 = 0$), △ ($\omega_1 = 0.189$) and ▽ ($\omega_2 = 0.408$) correspond most closely to the principal spectrum of longitudinal modes. Figure 14 presents the perturbation kinetic energy density K' and the local energy transfers $\mathscr{S}k$ and $\mathscr{S}t$ for the fastest growing mode labelled ◇ in figure 13, i.e. the ω_0 mode. The $\mathscr{S}t$ conversion is confined to the braids near the stagnation points and makes a small positive overall contribution to growth. The strongest $\mathscr{S}k$ conversion occurs along the inside edge of the braids and in the corners of the cat's eye where irrotational fluid is being entrained into the core. The maximum perturbation kinetic energy density K' is located exactly at the centre of the braids, indicating that the $\mathscr{S}t$ conversion has shifted the maximum K' away from the maximum $\mathscr{S}k$ conversion. The ω_1 and ω_2 modes have energy conversions that are essentially similar to those of the ω_0 component. The net $\langle \mathscr{S}t \rangle$ conversion is an order of magnitude smaller than the $\langle \mathscr{S}k \rangle$ term for all of the principal modes, which implies that the shearing deformation field provides the primary source of secondary instability for the maximum amplitude state of unstratified KH waves. (The values for the ω_0 mode are given in the caption.)

Figure 15 contains the K' fields for the other unstable modes shown in figure 13. The mode labelled ▷ resembles the ω_0 mode of the principal spectrum. It has zero angular frequency and its K' maxima are located near the stagnation points of the braids, although it has a pair of maxima associated with each stagnation point. The other modes are all confined to the central part of the vortex core. They appear to fall into three subclasses. Those with zero angular frequency exhibit a single tightly confined maximum of K' near the centre of the core. They will be denoted as C_0(○), C_0'(□), and C_0''(☆). These modes have been ordered according to their preferred spanwise wavenumber, with C_0 corresponding to the smallest ($d = 0.9$). Note also that the spatial scale of the K' field decreases from C_0 to C_0''. The central core modes with $\omega \sim 0.37 \pm 0.3$ (+ and ×) exhibit double peaks in the K' field, and are classified as $C_1(d = 0.6)$ and $C_1'(d = 1.4)$ respectively. The central core mode with $\omega \sim 0.73$ (●), which corresponds to C_2, has two maxima in the K' field and a localized circular minimum at the centre. Like the modes of the principal spectrum, these central core modes derive the major part of their kinetic energy from the $\langle \mathscr{S}k \rangle$ conversion, since the magnitude of the $\langle \mathscr{S}t \rangle$ term is less than 10% of σ in each case. In fact, some of the central core modes draw all of their growth from $\langle \mathscr{S}k \rangle$ conversion, since their $\langle \mathscr{S}t \rangle$ conversion is negative.

Some comparison of our results for $Ri = 0$ with previous work on the evolution of unstratified KH waves is in order. Using a semi-linear time-dependent model, Corcos & Lin (1984) have simulated the development of small-amplitude three-dimensional perturbations in the presence of an evolving two-dimensional KH wave with $Re = 100$ and $Ri = 0$. They have reported that the perturbation kinetic energy and energy conversions associated with secondary instability are strongest in the central part of the vortex core, which would correspond to the excitation of one of the central core modes in figures 13 and 15. They also found that streamwise vorticity appears in the braids as well as the vortex cores. Metcalfe *et al.* (1987) report the formation of streamwise vorticity along the braids in addition to the development of three-dimensional motions within the spanwise vortex cores for their fully nonlinear, three-dimensional simulations of a KH wave with $Ri = 0$. The growth rates and wavenumbers computed from their three-dimensional disturbance energy are comparable with the corresponding values for our fastest growing eigenmodes. For example, in the range $200 \leqslant Re \leqslant 400$, they find fastest growing modes with growth rates $0.09 \leqslant \sigma \leqslant 0.10$ and spanwise wavenumbers $1 \leqslant d \leqslant 2.4$. However, we note that their simulations most likely involve the excitation of a blend of the instabilities we have found, so a precise comparison is not possible.

Our linear stability analyses demonstrate that the three-dimensional motions which appear in the central part of the vortex core and near the braids originate as physically distinct secondary instabilities. Since the energy conversions for the ω_n and central core modes occur in different locations with little spatial overlap, it is clear that the modes can in fact grow independently of one another. The experiments of Lasheras & Choi (1988) and Breidenthal (1981), which report that three-dimensionality first appears along the braids, lend support to this distinction. Our

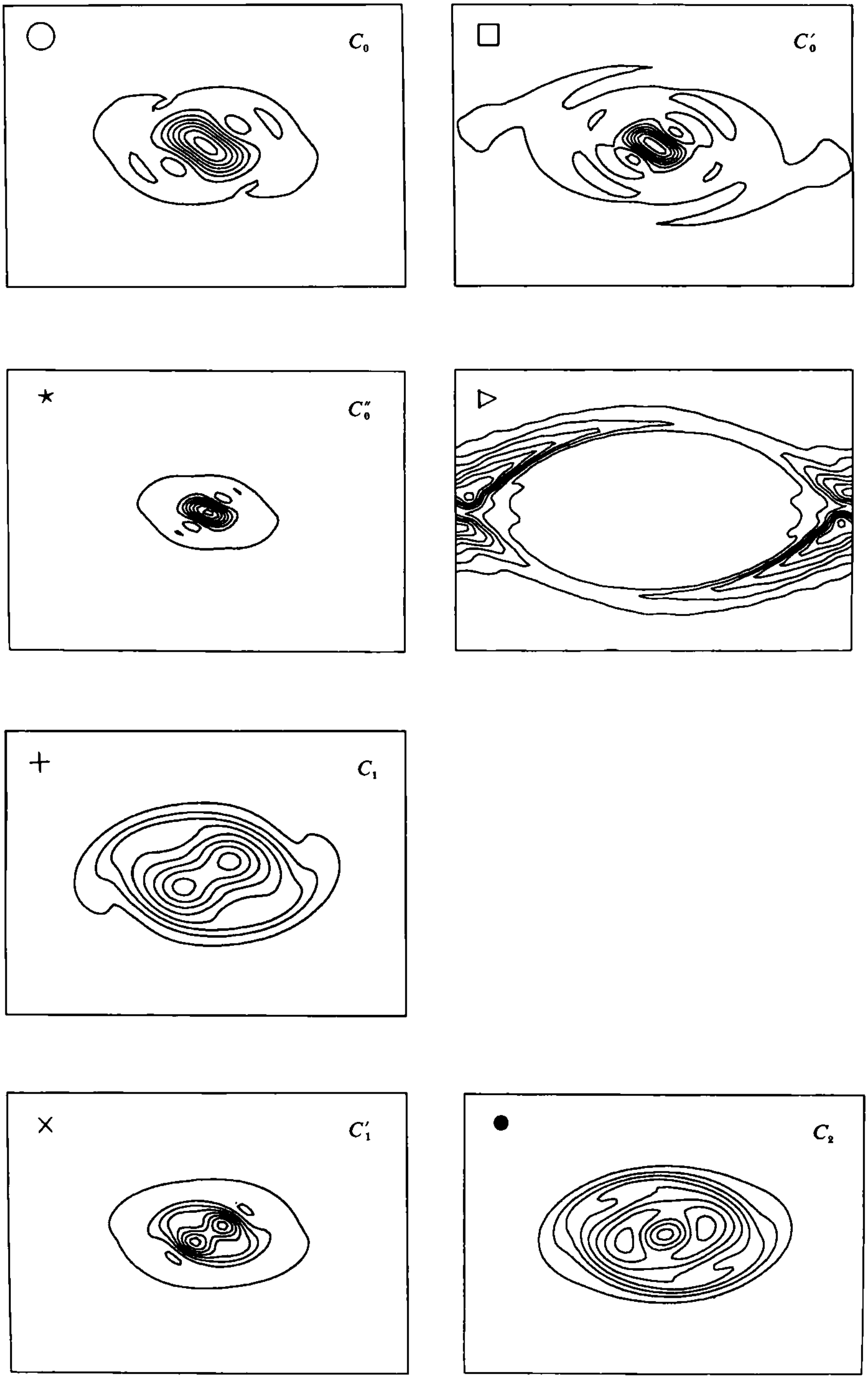

FIGURE 15. Kinetic energy density K' for various unstable modes of the maximum amplitude KH wave with $Ri = 0$ ($b = 0$). Each mode is labelled with the corresponding branch symbol shown in the corresponding σ *vs.* d plot (figure 13): (▷ $\omega = 0$, $d = 2.2$), (○ C_0, $\omega = 0$, $d = 0.9$), (□ C_0', $\omega = 0$, $d = 1.45$), (☆C_0'', $\omega = 0$, $d = 1.7$), (+C_1, $\omega = 0.356$, $d = 0.6$), (×C_1', $\omega = 0.396$, $d = 1.4$), (● C_2, $\omega = 0.725$, $d = 0.8$).

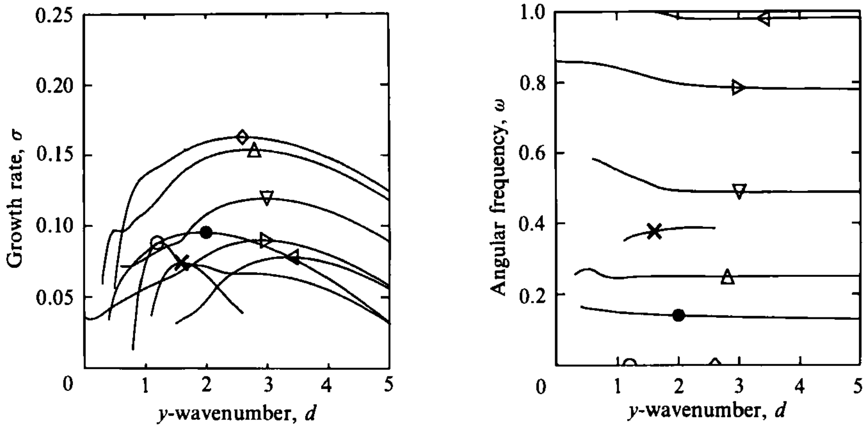

FIGURE 16. As for figure 13, except $Ri = 0.04$.

results indicate that the central core mode (C_0) actually onsets first, but its growth rate decays to a rather low level as the KH wave approaches maximum amplitude. It is superceded by the more rapidly growing longitudinal ω_0 mode (which introduces three-dimensional motions into the vicinity of the braids). The amplification factors we have estimated indicate that these two instabilities have a similar potential for growth (the early onset of C_0 compensates for its reduced rate of growth). Which of these secondary instabilities reaches nonlinear amplitude first is therefore likely to be sensitive to biases in the noise present in the layer at the time of its nonlinear roll-up.

Figure 16 presents the eigenvalues of the unstable longitudinal modes for the maximum amplitude KH wave state with $Ri = 0.04$. The modes labelled $\Diamond$ ($\omega_0 = 0$), $\triangle(\omega_1 = 0.250)$, ∇ ($\omega_2 = 0.489$), $\triangleright$ ($\omega_3 = 0.785$) and $\triangleleft$ ($\omega_4 = 0.980$) have been identified as members of the principal spectrum. The maximum growth rate of each of these branches is somewhat larger than their unstratified counterparts. The local energy transfers and the K' field for the fastest growing mode with $\omega_0 = 0$ are shown in figure 17 for $Ri = 0.04$. There are several important differences between this mode and the corresponding one for $Ri = 0$. For example, the $\mathscr{S}t$ conversion field is no longer associated with the strongest KH wave stretching deformation which is found in the braids, but rather occurs in the deep vorticity trough that lies just inside the braids. The maximum $\mathscr{S}h$ conversion is also no longer coincident with the braids. Instead, it is associated with the secondary maxima of the KH wave shearing deformation which are situated in the interior of the core at the lateral edges of the central vortex, adjacent to the irrotational entrainment troughs. Both of these changes are evidently due to the suppression of dynamical instability by positive static stability in that portion of the entrainment trough which is nearest to the braids. The KH wave shearing deformation is zero in the lid's of the cat's eye, so that the $\mathscr{S}h$ conversion is confined to the lateral edges of the vortex core. On the other hand, the $\mathscr{H}$ converts potential energy to kinetic energy in the eyelids but not at the edges of the vortex core, even though the stratification there is also superadiabatic. Evidently the strong vertical motions and shear present in these latter regions suppresses convective instability, so that the two major sources of energy for the instability operate in separate regions of the wave core.

Even though the growth rate of the ω_0 mode for $Ri = 0.04$ is larger than that of its unstratified counterpart, the net $\langle \mathscr{S}h \rangle$ and $\langle \mathscr{S}t \rangle$ terms are both slightly smaller for

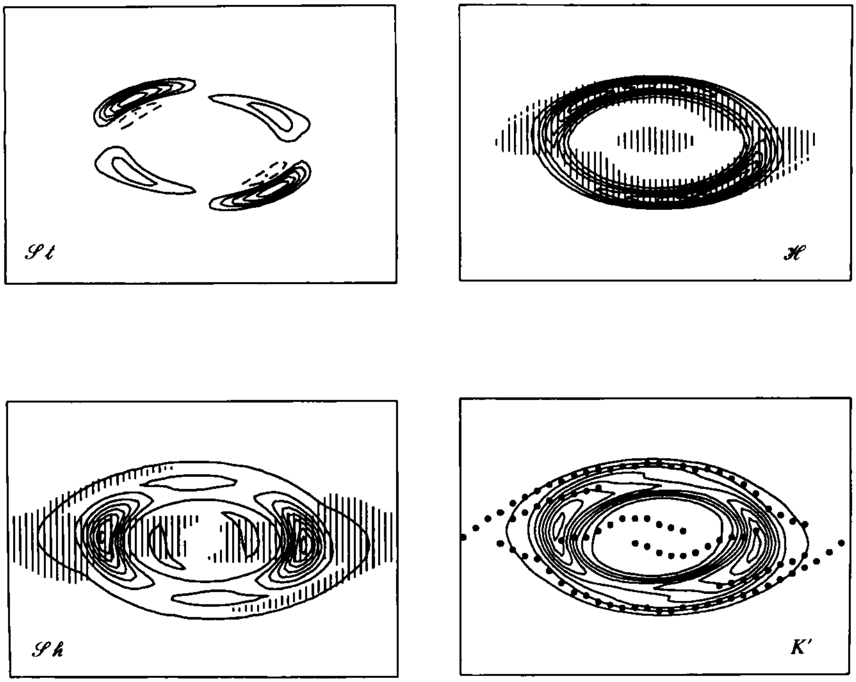

FIGURE 17. Eigenfunction correlations for the most unstable ω_0 mode (labelled ◇ in figure 16) of the maximum amplitude KH wave with $Ri = 0.04$. Here $t = 32$, $b = 0$, $d = 2.6$, $\sigma = 0.163$, $\omega = 0$. $\langle \mathcal{S}k \rangle = 0.110$, $\langle \mathcal{S}t \rangle = 0.010$, $\langle \mathcal{H} \rangle = 0.079$, $\langle \mathcal{D} \rangle = 0.036$ in units of $\langle K' \rangle$. The vertical heat flux $\mathcal{H}$ (x, z) is given by the integrand in (3.31). The superadiabatic region associated with the overturning fluid in the vortex core is marked with vertical lines superimposed on the $\mathcal{H}$ field. See figure 14 for further details.

$Ri = 0.04$. The increase in growth rate is therefore attributable to the positive contribution made by the vertical heat flux. The net $\langle \mathcal{S}k \rangle$ conversion is larger than the $\langle \mathcal{H} \rangle$ term, and the location of the maximum K' corresponds closely to that of the maximum $\mathcal{S}k$ conversion, implying that shear-driven dynamical instability is the primary source of energy for the mode. However, as noted above, it is clear that the presence of stratification has significantly altered the character of the mode. Furthermore, the close correspondence of the positive vertical heat flux, the shear conversion and the kinetic energy density with the superadiabatic region of the vortex core indicate the importance of contributions from convective forcing.

We have also been able to identify two central core modes for $Ri = 0.04$, namely $C_0(\bigcirc, \omega = 0)$ and $C_1(\times, \omega = 0.377)$ in figure 16. Their angular frequencies and kinetic energy distributions are similar to those of their unstratified counterparts. In addition to the $\mathcal{S}k$ conversions responsible for the growth of the latter, these stratified C_n modes derive energy from the formation of a secondary superadiabatic region at the centre of the vortex as the KH wave overturns for the second time. However, the $\langle \mathcal{S}k \rangle$ conversion is substantially stronger than the $\langle \mathcal{H} \rangle$, so it is clear that these modes are primarily dynamical in origin. Although the growth rates of the principal ω_n modes increased substantially with the addition of stratification, there is little or no corresponding increase in the growth rates of the C_n modes.

The stability properties of the maximum-amplitude KH wave state with $Ri = 0.08$ are very similar to those found at $Ri = 0.12$, so we shall present only the latter in figure 18. The principal modes for $Ri = 0.12$ are ◇ $(\omega_0 = 0)$, △ $(\omega_1 = 0.204)$, ▽

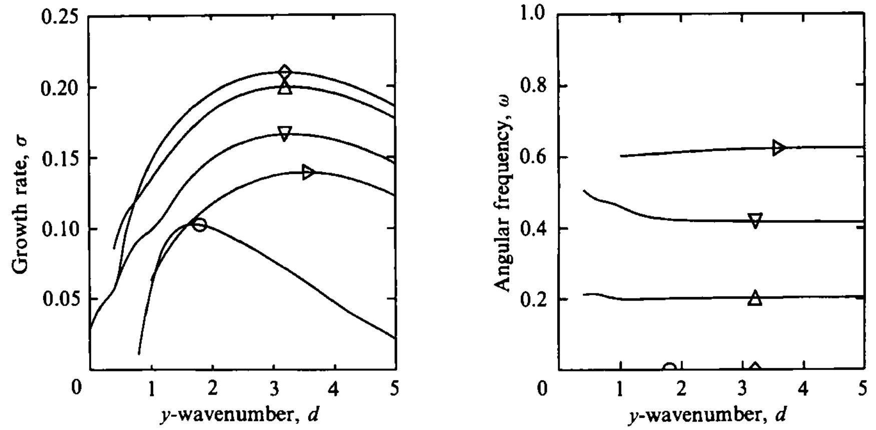

FIGURE 18. As for figure 13, except $Ri = 0.12$.

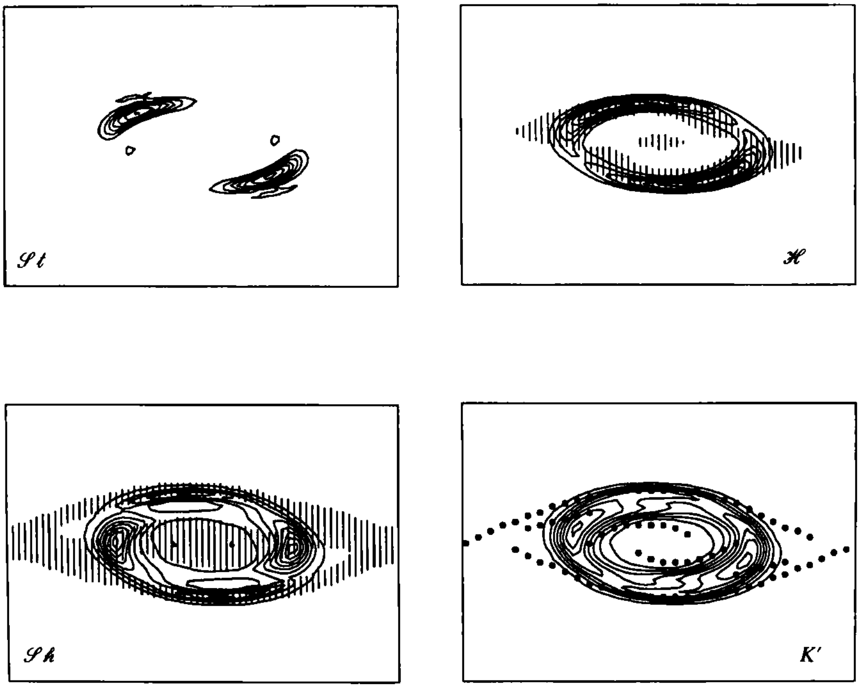

FIGURE 19. Eigenfunction correlations for the most unstable ω_0 mode (labelled ◇ in figure 18) of the maximum amplitude KH wave with $Ri = 0.12$. Here $t = 42$, $b = 0$, $d = 3.2$, $\sigma = 0.210$, $\omega = 0$. $\langle \mathscr{S}k \rangle = 0.119$, $\langle \mathscr{S}t \rangle = 0.020$, $\langle \mathscr{H} \rangle = 0.128$, $\langle \mathscr{D} \rangle = -0.058$ in units of $\langle K' \rangle$. See figures 14 and 17 for further details.

($\omega_2 = 0.419$), and ▷ ($\omega_3 = 0.624$). (For comparison purposes, the frequencies of the first four members of the $Ri = 0.08$ principal spectrum are $\omega_0 = 0$, $\omega_1 = 0.243$, $\omega_2 = 0.484$, and $\omega_3 = 0.780$.) The non-oscillatory mode (labelled ○, $\omega = 0$) is a C_0 central core mode and has a K' field which resembles that of the corresponding mode shown in figure 15 for $Ri = 0$. The growth rates of the most unstable principal modes for $Ri = 0.08$ and 0.12 are greatly increased relative to their counterparts at lower

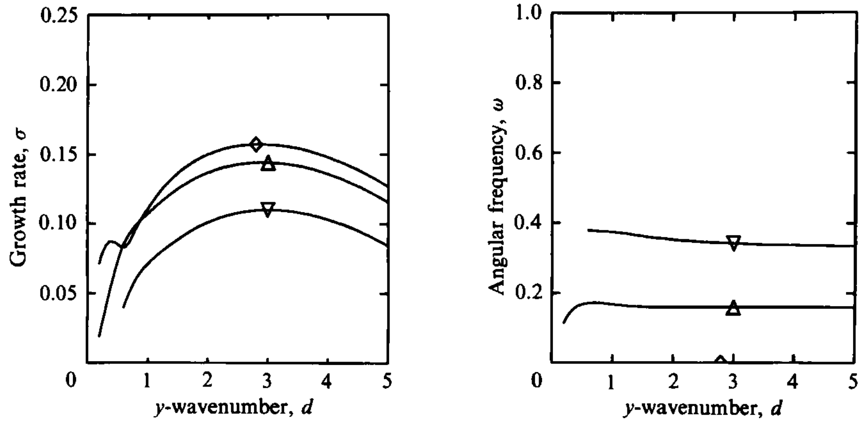

FIGURE 20. As for figure 13, except $Ri = 0.16$.

values of the stratification. In what follows, we shall demonstrate that this is due to an increase in the $\langle \mathscr{H} \rangle$ conversion term, which exceeds both the $\langle \mathscr{S}k \rangle$ and $\langle \mathscr{S}t \rangle$ terms. This means that the primary source of kinetic energy for these principal modes at the time of maximum wave kinetic energy is convective activity, i.e. the conversion of potential to kinetic energy in the superadiabatic region at the upper and lower edges of the KH wave core.

Figure 19 shows that the nature of the $\mathscr{S}k$ conversion for $Ri = 0.12$ is somewhat different from that for $Ri = 0.04$ ($Ri = 0.08$ is similar to 0.04 and therefore has not been shown). The $Ri = 0.12$ $\mathscr{S}k$ conversion field contains thin layers of production in the uppermost and lowermost sections of the braids near $x = \frac{1}{2}\lambda_{\mathrm{KH}}$ which are not present at lower values of the stratification. These regions of $\mathscr{S}k$ production lie just outside the extreme upper and lower boundaries of the primary superadiabatic region and are clearly associated with baroclinic enhancement of the KH wave shearing deformation field in that region.

Figure 20 contains the eigenvalues of unstable longitudinal modes for the maximum-amplitude KH wave state with $Ri = 0.16$. The eigenmodes of the principal spectrum, which are labelled ◇ ($\omega_0 = 0$), △ ($\omega_1 = 0.159$) and ▽ ($\omega_2 = 0.343$) have growth rates that are substantially smaller than the corresponding modes at $Ri = 0.08$ and 0.12. For $Ri = 0.16$ the $\langle \mathscr{S}k \rangle$ conversion dominates the contributions to the growth rate, although the $\langle \mathscr{H} \rangle$ term still makes a significant contribution. The net $\langle \mathscr{S}t \rangle$ conversion is negative for this level of stratification. As in the case of $Ri = 0.12$, the $\mathscr{S}k$ conversion field of the ω_0 mode shown in figure 21 possesses thin layers of production in the uppermost and lowermost sections of the braids in addition to those at the lateral edges of the central vortex.

4.3. *Summary of stratification effects*

Figure 22 illustrates the manner in which the growth rate σ, the angular frequency ω, and the spanwise wavenumber d of the fastest growing mode from each of the ω_0, ω_1 and ω_2 branches varies with the Richardson number. For all three modes of instability, the strongest growth occurs between the Richardson numbers 0.08 and 0.12. The growth rates of these secondary instabilities also extrapolate to zero at $Ri \approx 0.22$, which is close to the cutoff value $Ri = 0.25$ for the primary KH instability. The angular frequencies do not vary substantially with Ri which lends support to our implicit assumption that the modes of the principal spectrum are related and vary

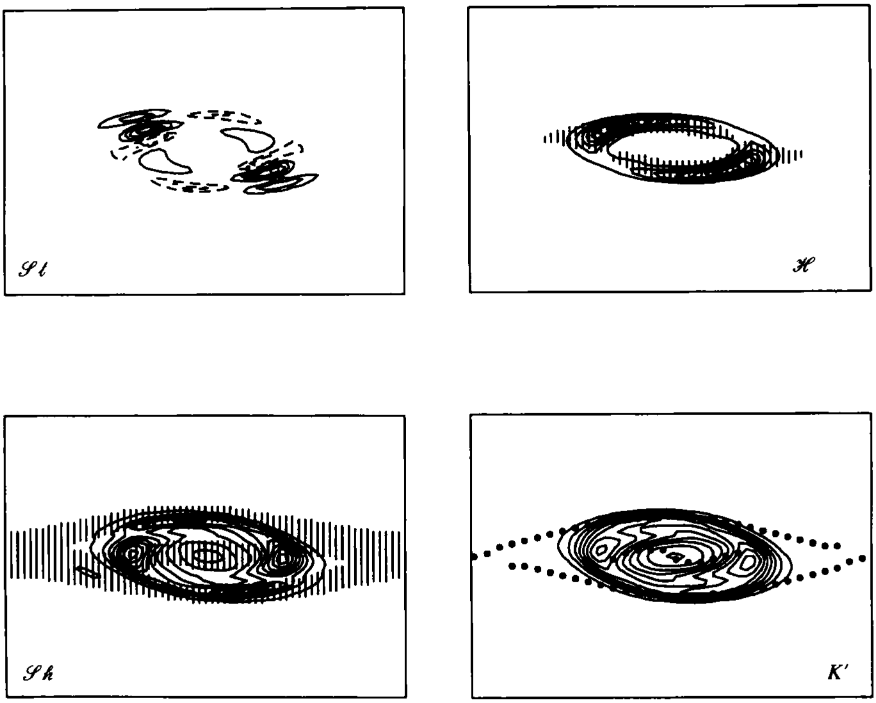

FIGURE 21. The most unstable ω_0 mode (labelled ◇ in figure 20) of the maximum amplitude KH wave with $Ri = 0.16$. Here $t = 52$, $b = 0$, $d = 2.8$, $\sigma = 0.157$, $\omega = 0$. $\langle \mathcal{S}k \rangle = 0.138$, $\langle \mathcal{S}t \rangle = -0.003$, $\langle \mathcal{H} \rangle = 0.068$, $\langle \mathcal{D} \rangle = -0.045$ in units of $\langle K' \rangle$. See figures 14 and 17 for further details.

smoothly with the initial stratification. The preferred spanwise wavenumbers increase sharply from $Ri = 0$ to 0.04, but do not vary greatly for the larger values of stratification we have considered. This sharp increase in the preferred value of d coincides with the introduction of an accessible reservoir of potential energy as an important source of secondary instability. Note that the wavenumber bandwidth of these instabilities is rather broad (as shown in figures 13, 16, 18, and 20), so that the spanwise wavenumbers presented in figure 22 are not strongly preferred. We also note that the ω_1 mode grows nearly as quickly as the ω_0 mode, so that we cannot exclude the possibility that motions of characteristic angular frequency ω_1 could be introduced into the layer. (See Klaassen & Peltier 1985*b* for a discussion of the relevant amplification factors for $Ri = 0.07$.)

Figure 23 shows the Richardson-number dependence of the net energy conversions $\langle \mathcal{S}k \rangle$, $\langle \mathcal{S}t \rangle$, $\langle \mathcal{H} \rangle$ and $\langle \mathcal{D} \rangle$ corresponding to the most unstable ω_0 and ω_1 modes displayed in figure 22. The $\langle \mathcal{H} \rangle$ term shows the greatest variation with Ri, being zero for $Ri = 0$, increasing to a maximum near $Ri = 0.11$ and decreasing sharply for larger Ri. Since the other conversion terms exhibit only minor variations with Ri, these changes in the $\langle \mathcal{H} \rangle$ are clearly responsible for the major part of the growth rate variations shown in figure 22. The $\langle \mathcal{H} \rangle$ contributions to growth exceed the $\langle \mathcal{S}k \rangle$ contributions in the range $0.065 \leqslant Ri \leqslant 0.13$, indicating that convective activity is the principal source of instability for this range of Ri. This is consistent with the conclusion reached by Klaassen & Peltier (1985*b*, *c*) regarding the convective nature of the most unstable mode of KH waves with $Ri = 0.07$, although we note that the net $\langle \mathcal{S}k \rangle$ conversion term makes a more significant contribution to the

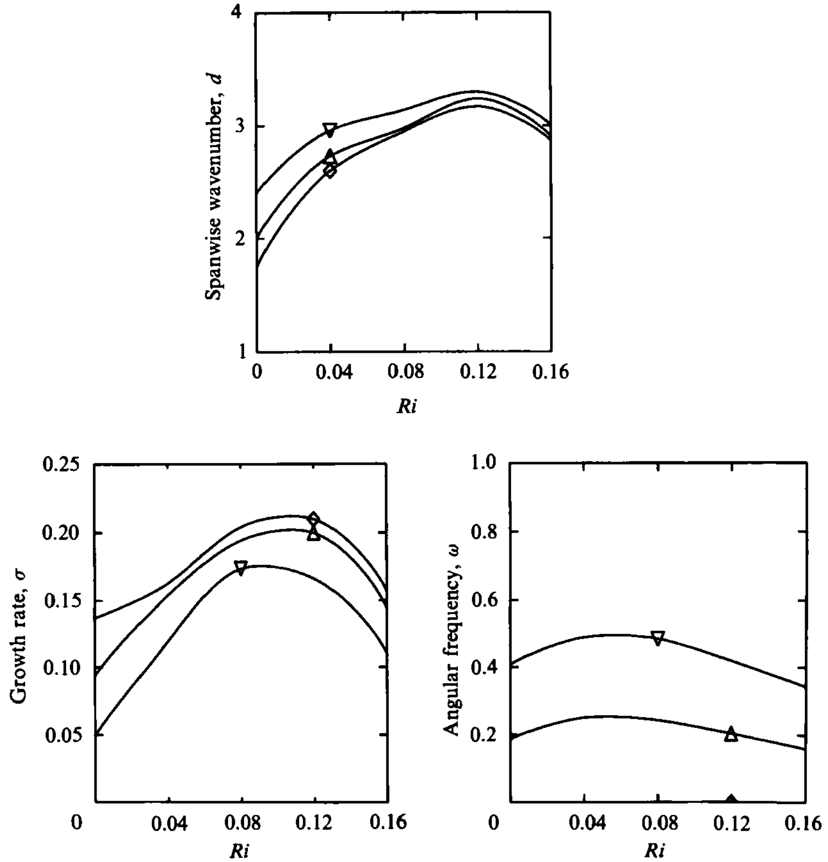

FIGURE 22. The effect of bulk Richardson number Ri on the most unstable ω_0 (◇), Ω_1 (△), and ω_2 (▽) modes of the maximum amplitude KH wave state. For Floquet parameter $b = 0$.

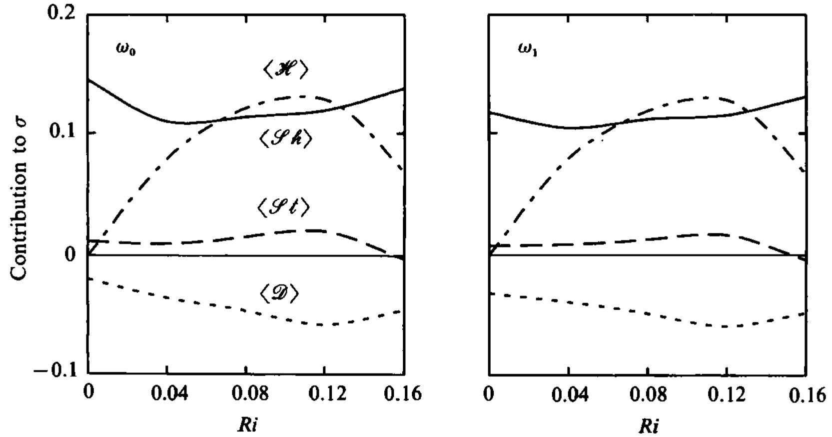

FIGURE 23. The effect of Ri on energy conversions for the most unstable ω_0 and ω_1 modes. See figure 11 for further details.

growth rate than had been anticipated. In fact, stratification evidently has only a small effect on the rather substantial absolute contribution made by $\langle \mathscr{S}k \rangle$ to the growth rate. This implies that KH waves evolving in shear layers possessing different initial stratification share a common source of secondary shear instability associated with the nonlinear development of the vortex.

Since one might have expected stronger stratification to increase the amount of potential energy released during overturning, the decrease of $\langle \mathscr{H} \rangle$ and σ as *Ri* increases above 0.11 warrants further discussion. Figures 3 and 4 clearly show that baroclinic effects increase the vorticity and shearing deformation present in the braids of the KH waves as *Ri* increases, while weakening that found in the central vortex. As *Ri* increases above 0.11, these changes in KH wave structure lead to a decrease of $\langle \mathscr{S}k \rangle$ conversion in the lateral edges of the vortex core, and an increase in the 'eyelid' portion of the braids. Since these changes compensate each other, the $\langle \mathscr{S}k \rangle$ conversion does not vary greatly. However, these changes in KH wave structure do lead to significant changes in $\langle \mathscr{H} \rangle$. The growth rate of a convective instability depends on the Rayleigh number, which is proportional to the density difference across the superadiabatic layer, and also to the depth of the layer *cubed*. As may clearly be seen from figures 17, 19 and 21, the reduction in principal mode growth rates for $Ri \geqslant 0.11$ is associated with a decrease in the depth of the superadiabatic region, which is in turn a consequence of the smaller vertical amplitude of the vortex as well as the increased strength of the braids in the lids of the cat's eye.

5. Comparison with other models of secondary instability

Pierrehumbert & Widnall (1982) (hereinafter referred to as PW82), found that Stuart vortices were subject to three-dimensional translative instability, and that for an amplitude of $A = 0.25$, the preferred spanwise wavenumber was $d = 1.6$ (in our units). (Owing to the different non-dimensional scaling employed, the growth rates, angular frequencies and wavenumbers of PW82 must all be divided by two for comparison with ours.) Pierrehumbert (1986) later established that translative instability was closely related to the instability of a constant elliptical vortex. In order to explore the relation between the central core instabilities we have found for KH waves and these model secondary instabilities, we have repeated the PW82 calculations, employing considerably greater resolution than was apparently possible in this earlier study.

Figures 24 and 25 show our results for a Stuart vortex with amplitude $A = 0.25$ employing truncation levels $N = 15$, 23 and 35. The branch labelled $\Diamond$ has angular frequency $\omega = 0$ and corresponds to the translative instability reported by PW82. The growth rates we obtain for this branch at $N = 15$ (somewhat higher resolution than was used by PW82) are very close to those obtained by PW82 for all values of the spanwise wavenumber. However, as the truncation parameter is increased from $N = 15$ to $N = 35$, the translative ($\Diamond$) growth rates decrease for $d < 2.5$, and faster growing non-oscillatory modes appear at those wavenumbers.

In figure 25 there are three values of spanwise wavenumber, namely $d = 2.15, 2.75$ and 3.65, for which the various branches having $\omega = 0$ possess nearly degenerate eigenvalues $s = \sigma + \mathrm{i}\omega$. At these points the numerical eigenvalue algorithm experiences difficulty in distinguishing the nearly degenerate modes, and may produce slight errors in the corresponding eigenvalues. We have performed a sufficient number of calculations to establish that the $\omega = 0$ curves at $d = 2.15$ and

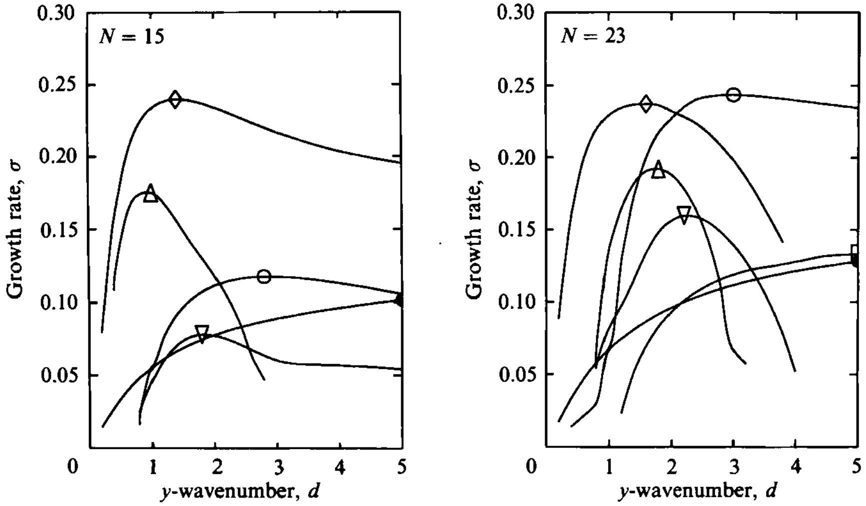

FIGURE 24. Growth rate σ *vs.* spanwise wavenumber d for a Stuart vortex of amplitude $A = 0.25$, shown for truncation levels $N = 15$ and 23. The symbols on each branch denote the fastest growing mode. For $N = 15$ the angular frequencies of the fastest growing modes in each branch are: ◇, $\omega = 0$; △, $\omega = 0.40$; ▽, $\omega = 0.85$; ○, $\omega = 0$; ●, $\omega = 0$. For $N = 23$, they are: ◇, $\omega = 0$; △, $\omega = 0.54$; ▽, $\omega = 1.02$; ○, $\omega = 0$; ●, $\omega = 0$.

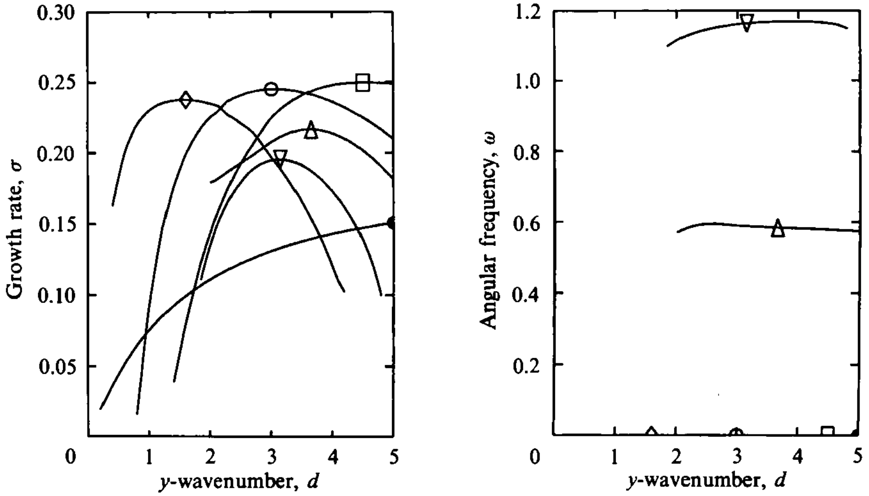

FIGURE 25. Growth rate σ and angular frequency ω *vs.* spanwise wavenumber d for a Stuart vortex of amplitude $A = 0.25$, shown for truncation level $N = 35$. The Floquet parameter $b = 0$. The angular frequencies of the fastest growing modes in each branch are: (T_0: ◇, $\omega = 0$); (T_1: △, $\omega = 0.58$); (T_2: ▽, $\omega = 1.16$.) The modes T_0'(○), T_0''(□), and ● all have $\omega = 0$.

2.75 do not cross for $N = 35$. However, a detailed examination of the eigenfunctions for several intermediate values of d indicates that the curves labelled ◇, ○ and □ represent three distinct modes of instability. It is therefore clear that the curves in question must cross in the limit of infinite truncation and they have been presented that way in figure 25. In what follows we shall refer to these three modes (in order of increasing preferred spanwise wavenumber) as T_0 (translative ◇), T_0' (○), and T_0'' (□).

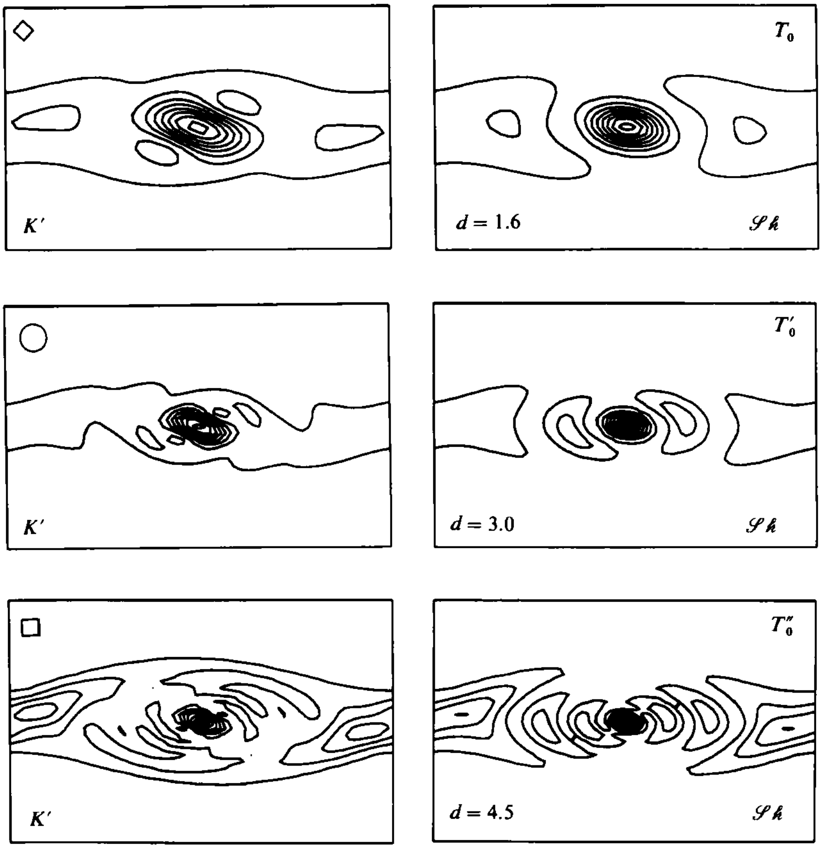

Figure 26. For caption see facing page.

The kinetic energy K' and the $\mathscr{S}k$ conversion of the T_0 mode (figure 26) show that it is confined to the central part of the vortex. The modes T_0' and T_0'', which were not reported in PW82, also correspond to instabilities of the central vortex core, and are clearly related to the translative mode T_0. The T_0' branch has a larger maximum growth rate ($\sigma = 0.245$) and a larger preferred wavenumber ($d = 3.0$) than the T_0 branch ($d = 1.6, \sigma = 0.238$). As one might expect from the shorter preferred spanwise scale, the kinetic energy K' of T_0' is confined to a smaller region of the vortex core than is T_0. The T_0'' branch has a maximum σ of 0.250 and preferred d of 4.5, which are both larger than either of the corresponding values for T_0 and T_0'. The central maxima of the K' and $\mathscr{S}k$ correlations of the T_0'' mode are even more narrowly confined to the central part of the vortex core.

Our results suggest the possible existence of further modes in the sequence T_0, T_0', T_0'', …, each possessing increasingly smaller spatial scales and larger growth rates. If this were true, it would imply (in contrast to the PW82 result of $d = 1.6$) a very small and possibly infinitesimal spatial scale for the most unstable mode of the inviscid Stuart vortex. As argued previously by Pierrehumbert (1986) for the simpler case of a constant elliptical vortex, it would also imply the existence of a mechanism for injecting energy directly from the large-scale vortex into the dissipation range. It is interesting that the injection mechanism for the constant elliptical vortex consists of a single mode having maximum growth in the limit of infinite spanwise wavenumber, whereas in the Stuart vortex case, it consists of a sequence of distinct modes, each

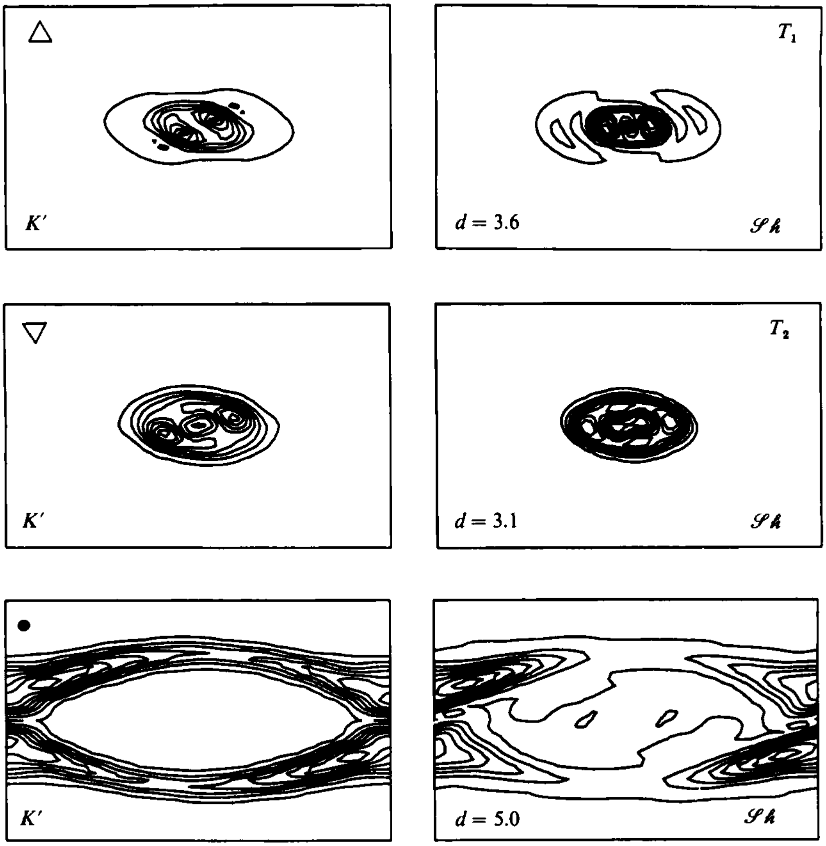

FIGURE 26. Eigenfunction correlations K' and $\mathscr{S}k$ for the unstable modes of a Stuart vortex of amplitude $A = 0.25$ for $b = 0$. Each mode is labelled with the corresponding branch symbol shown in figure 25. For the modes shown, $\mathscr{S}k$ conversion comprises the dominant contribution to growth. In all cases the net $\langle \mathscr{S}k \rangle$ conversion was negative and less than 2.5% of the $\langle \mathscr{S}k \rangle$ contribution in magnitude. The horizontal domain length is 2π, while the height shown is 4.

possessing successively shorter preferred wavelengths. It is tempting to speculate that the additional modes in the Stuart vortex sequence might owe their existence to the finite extent of the parent vorticity distribution.

The kinetic energy and $\mathscr{S}k$ conversion correlations shown in figure 26 demonstrate that the fastest growing modes of the branches labelled △ and ▽ are also confined to the central part of the vortex core. Those modes labelled △ correspond to a higher-order modes like the one displayed in figure 10 of PW82 for $A = 0.2$, although it should be understood that the PW82 mode is for $b = \frac{1}{2}\alpha$, whereas ours is for $b = 0$. For $N = 35$, the branch labelled △ has angular frequency $\omega \approx 0.58$ and exhibits a double peak of kinetic energy near the vortex centre, while the branch labelled ▽ has $\omega \approx 1.16$ and three extrema of K'. The similarity between the correlations of these two modes and those for the translative mode T_0 implies that they form the fundamental and first harmonic of a Fourier spectrum which has the T_0 mode as its non-oscillatory component. If we denote the △ branch as T_1 and the ▽ branch as T_2, then we may refer to the spectrum of translative modes as T_n, where the angular frequency of the members is given by $\omega_n = n\Omega_T$, where $\Omega_T \approx 0.58$ for $A = 0.25$. The fact that the angular frequencies of the unstable branches of both unsteady KH and steady Stuart vortices form the first few components of a Fourier spectrum is significant, since it implies that this particular characteristic is not associated with the temporal variability of the vortex.

The estimated errors for the maximum eigenvalues of the T_0, T_0' modes are less than 1%. It is evident from figures 24, 25 and 26 that, owing to the small spatial scales involved, a similarly high degree of convergence has not been obtained for the T_0'', T_1 and T_2 modes. By performing a few calculations at truncation levels higher than $N = 35$, we have estimated that the errors in the eigenvalues of the most unstable T_0'', T_1 and T_2 modes are on the order of 10%. (The best estimates we have for the frequencies are $\omega(T_1) = 0.61$ and $\omega(T_2) = 1.2$ for $N = 41$.) It should be mentioned that the error in the preferred values of d for T_1, T_2 are probably somewhat larger than those for s. Consequently the T_1 and T_2 modes have been included here only for the purpose of qualitative comparison with the KH case. We note that other branches of instability (including a possible T_0''') have been found in our calculations, but did not exhibit a sufficient degree of convergence to warrant further discussion.

We recall that secondary instabilities confined to the centre of the vortex core have also been found in §4 for the more realistic case of a viscous, unstratified KH billow. In fact, a comparison of the relevant eigenfunction correlations in figures 15 and 26 demonstrates that there is a one-to-one correspondence between the KH wave central core modes C_0, C_0', C_0'', C_1, C_2 and the T_0, T_0', T_0'', T_1, T_2 modes of the Stuart vortex.

The close correspondence between the eigenfunction correlations of the Stuart vortex and KH central core modes strongly suggests that a common mechanism is responsible for both. Since Pierrehumbert (1986) has established that the Stuart vortex translative instability (i.e. T_0) is associated with the ellipticity of the vorticity distribution, it would seem reasonable to identify the central core modes C_n of the KH wave as manifestations of the instability of an elliptical vortex. This identification should be qualified by noting that there are some differences between the KH and Stuart vortex cases. The preferred spanwise wavenumbers of the KH central core modes are somewhat smaller than those for the Stuart vortex, presumably owing to the longer wavelength of the KH vortex and the influence of viscosity. Secondly, viscous dissipation causes the growth rates of the preferred KH central core branches to decrease with increasing preferred spanwise wavenumber (the opposite of the inviscid Stuart vortex case). Thirdly, the T_1' mode corresponding to the KH instability of C_1' shown in figure 15 has not been found among the resolved unstable modes of the Stuart vortex with $A = 0.25$.

For the KH wave states with positive values of Ri that we have examined here, we have been unable to identify secondary central vortex core instabilities corresponding to many of the higher-order Stuart vortex modes (in particular, T_2, T_0', T_0''). For $Ri = 0.04$, the modes labelled ○(C_0) and $\times\,(C_1)$ in figure 16 correspond to the T_0 and T_1 instabilities, respectively. For $Ri = 0.12$, the branch labelled ○(C_0) in figure 18 corresponds to the T_0 mode. We have also found a C_0 mode for the KH wave for $Ri = 0.16$, but by the time the nonlinear wave climaxes, its growth rate has decayed to a very low value. The results shown in §4 indicate that the C_0 mode may be able to compete with the ω_0 mode in the unstratified case, but that it is unlikely to do so for the stratified waves we have considered.

Figure 26 shows that the unstable Stuart vortex mode labelled ● is distinctly different from the T_n modes in that it is not confined to the central region of the vortex core. Instead, this mode, which has angular frequency $\omega = 0$, is confined to a doubly connected region that surrounds the vortex centre and encompasses the stagnation points. Its K' field has four maxima located directly above and below the stagnation points of the Stuart vortex, which implies that it is more closely related to the secondary KH instability labelled ▷ in figure 15 than it is to ω_0. (The latter mode has two dominant K' maxima which are located toward the sides of the stagnation points which contain the entrainment troughs.) These modes (●, ▷) might possibly be classified as ω_0', but it should be noted that we have been unable to establish the existence of stratified counterparts, or other unstratified modes which might correspond to ω_0'', ω_1', etc. This is not particularly important, however, since the ▷ KH mode has a comparatively low growth rate, and is not likely to play a significant role in the growth of secondary disturbances in free shear layers.

It is significant that we have not been able to identify any resolved unstable modes of the Stuart vortex which correspond directly to the principal spectrum of secondary KH instabilities, especially since we have established that the principal ω_0 mode plays a prominent role in the development of three-dimensional disturbances in two-dimensional KH waves. Although there appears to be a close correspondence between the central core modes of KH waves and Stuart vortices, the fact remains that the central core modes constitute only a subset of the available secondary instabilities of KH waves. Furthermore, the principal ω_0 mode plays a prominent role in the instability of unstratified KH waves, and fully dominates the secondary stability properties of stratified KH waves. Clearly, the fact that the Stuart vortex does not entrain irrotational fluid into its core limits its usefulness as a model of shear-layer dynamics.

6. Discussion

This paper has focused on two classes of secondary instabilities which may introduce three-dimensional disturbances into two-dimensional Kelvin–Helmholtz flow. The first class comprises modes which remain confined to the central part of the vortex core and are evidently related to the instability of an elliptical vortex. For all levels of stratification we have considered, these central core modes derive the major part of their growth from shearing conversion. They onset relatively early in the development of the KH wave, but tend to decay as the wave approaches maximum amplitude. The amplification factors we have calculated indicate that the central core modes are likely to make significant contributions to the development of three-dimensional motions only when the stratification is weak. The second class of instabilities, which we have referred to as the principal spectrum, derives its growth from the interface between strongly rotational and weakly rotational fluid (particularly in the vicinity of the entrainment troughs, where the deformation field is strong). In the stratified case, energy is also derived from convective motions in the statically unstable regions which develop as the interface between the two streams overturns. The principal modes onset somewhat later than the central core modes and achieve maximum growth as the nonlinear wave climaxes. These modes initially derive the major part of their growth from shearing conversion, but at the time of maximum wave amplitude, vertical heat flux confined to the superadiabatic region represents the primary source of perturbation kinetic energy for KH waves with $0.065 \leqslant Ri \leqslant 0.13$. For each level of stratification the amplification factor of the dominant non-oscillatory principal mode indicates that it will lead to the development of large-amplitude three-dimensional motions in the outer regions of the vortex core.

Our analyses have established that the stratified and unstratified secondary instabilities have much in common, especially in the early stages of development when the shear conversion provides the dominant source of growth. The fact that the absolute contribution of the shearing deformation – Reynolds stress term $\langle \mathscr{S}\mathscr{k} \rangle$ to the growth rate of secondary instability does not vary substantially with the initial stratification of the layer suggests that dynamical shear instability forms a fundamental contribution to the onset of three-dimensional motions in all free shear layers. However, we have shown that the introduction of stratification significantly modifies this basic shear instability. For the values of *Ri* we have considered, these modifications include a shifting of the maximum shearing conversion away from the braids and toward the lateral edges of the vortex core, an increase in growth rate associated with the conversion of potential to kinetic energy in the superadiabatic regions of the core, as well as an increase in spanwise wavenumber. The shifting of maximum shearing conversion with increasing stratification is due to the introduction of stable stratification along the braids and the adjacent portions of the entrainment troughs.

This coexistence of secondary dynamical and convective instabilities is not particularly surprising when one recognizes that the nonlinear development of the primary wave involves the entrainment of two fingers of nearly irrotational fluid into the vortex core. For stratified flow, one of these fingers contains light fluid from the upper layer, while the other contains heavy fluid from the lower layer. As the vortex rolls up, these two fingers become intertwined with the strongly rotational fluid at the centre of the layer. Strong shear and density gradients are therefore found along the braids and in the spiral interface between these two fluid fingers, so one might expect that both shear and convective instabilities could be excited there. Note, however, that the site of strongest dynamical instability is in the lateral edges of the cat's eye where the KH wave deformation is large, while the convective instability is confined to the 'lids' of the cat's eye where superadiabatic stratification exists.

We have extended the Stuart vortex stability analyses of Pierrehumbert & Widnall (1982) to considerably higher truncation levels and found several different types of secondary stability not reported in the PW82 study. The translative mode found in PW82 is not the most unstable. The similarities between the Stuart vortex instabilities and the KH central core modes strongly suggests that the three-dimensional motions found in the central part of the vortex core of unstratified KH billows are due to a secondary instability of the translative type and, by inference, to the elliptical instability described by Pierrehumbert (1986). The calculations reported here indicate that the Stuart vortex model captures only a subset of the instabilities to which more realistic nonlinear waves are subject. In fact we have not been able to find any resolved secondary instabilities of Stuart vortices that correspond directly to modes of the principal KH spectrum, although we cannot exclude the possibility that some modes which are not resolved by the present calculations may fulfil that role.

Finally, the calculations we have presented have elucidated the nature of secondary instabilities in the unstratified case. Corcos & Lin (1984) found that the maximum kinetic energy associated with three-dimensional perturbations occurred at the centre of the vortex and that this value was several times larger than the maximum level found in the braids. They attributed the three-dimensional motions in the vortex core to translative instability. Our calculations have demonstrated that this interpretation is correct, at least for the central part of the vortex core. They also reported the occurrence of streamwise vorticity in the braids, and that this vorticity was somewhat stronger than that found in the vortex core. Metcalfe *et al.* (1987)

found that strong three-dimensional motions occurred in the vicinity of the braid stagnation points as well as in the vortex core. They were not able to distinguish whether these developments were related or completely independent. Our stability analyses have revealed that both types of secondary instability exist independently. Although the secondary instability confined to the central part of the vortex core onsets first, its rate of growth is superseded by that of the principal mode. Our calculations indicate that this latter instability will lead to the development of three-dimensional motions near the braid stagnation points. The central core mode, on the other hand, may experience a significant fraction of its growth during the period in which the KH wave is rapidly growing, and consequently our estimates concerning its overall amplification are necessarily imprecise. However, the calculations do indicate that the central core mode is likely to experience roughly the same overall amplification as the principal mode. The fastest growing central core mode has a longer preferred spanwise wavelength compared to the principal mode. Thus, the choice of spanwise scale for a numerical model intended to simulate the onset of these disturbances, or the nature of the initial small-amplitude fluctuations employed to excite the instability could lead to a preference for either one or the other of these various 'routes to chaos'.

This research was supported through grants from the Natural Sciences and Engineering Research Council and the Atmospheric Environment Service of Canada. The calculations were carried out on the CRAY X-MP/24 at the Ontario Centre for Large Scale Computation and the manuscript was typed by Marion Stasiuk.

REFERENCES

BAYLY, B. J., ORSZAG, S. A. & HERBERT, T. 1988 Instability mechanisms in shear-flow transition. *Ann. Rev. Fluid Mech.* **20**, 359–391.

BERNAL, L. P. & ROSHKO, A. 1986 Streamwise vortex structure in plane mixing layers. *J. Fluid Mech.* **170**, 499–525.

BREIDENTHAL, R. E. 1981 Structure in turbulent mixing layers and wakes using a chemical reaction. *J. Fluid Mech.* **109**, 1–24.

BROWAND, F. K. 1966 An experimental investigation of the instability of an incompressible separated shear layer. *J. Fluid Mech.* **26**, 281–307.

BROWAND, F. K. & WINANT, C. D. 1973 Laboratory observations of shear-layer instability in a stratified fluid. *Boundary-Layer Met.* **5**, 67–77.

BROWN, G. L. & ROSHKO, A. 1974 On density effects and large scale structure in turbulent mixing layers. *J. Fluid Mech.* **64**, 775–816.

CORCOS, G. M. & LIN, J. S. 1984 The mixing layer: deterministic models of a turbulent flow. Part 2. The origin of the three-dimensional motion. *J. Fluid Mech.* **139**, 67–95.

DAVIS, P. A. & PELTIER, W. R. 1979 Some characteristics of the Kelvin–Helmholtz and resonant overreflection modes of shear flow instability and of their interaction through vortex pairing. *J. Atmos. Sci.* **36**, 2395.

FREYMUTH, P. 1966 On transition in a separated laminar boundary layer. *J. Fluid Mech.* **25**, 683–704.

HO, C.-M. & HUERRE, P. 1984 Perturbed free shear layers. *Ann. Rev. Fluid Mech.* **16**, 365–424.

JIMENEZ, J., COGOLLOS, M. & BERNAL, L. P. 1985 A perspective view of the plane mixing layer. *J. Fluid Mech.* **152**, 125–143.

KLAASSEN, G. P. 1991 Subharmonic secondary instabilities in free shear layers. *Geophys. Astrophys. Fluid Dyn.* (*sub judice*).

KLAASSEN, G. P. & PELTIER, W. R. 1985*a* The evolution of finite amplitude Kelvin–Helmholtz billows in two spatial dimensions. *J. Atmos. Sci.* **42**, 1321–1339.

KLAASSEN, G. P. & PELTIER, W. R. 1985*b* The onset of turbulence in finite amplitude Kelvin–Helmholtz billows. *J. Fluid Mech.* **155**, 1–35.

KLAASSEN, G. P. & PELTIER, W. R. 1985*c* The effect of Prandtl number on the evolution and stability of finite amplitude Kelvin–Helmholtz billows. *Geophys. Astrophys. Fluid Dyn.* **32**, 23–60.

KLAASSEN, G. P. & PELTIER, W. R. 1987 Secondary instability and transition in finite amplitude Kelvin–Helmholtz billows. In *Proc. Third Intl Symp. on Stratified Flows. Feb. 3–5, 1987, Pasadena, CA*, vol. I. (Reprinted in *Stratified Flows* (ed. E. J. List & G. H. Jirka). *ASME.*)

KLAASSEN, G. P. & PELTIER, W. R. 1989 The role of transverse secondary instabilities in the evolution of free shear layers. *J. Fluid Mech.* **202**, 367–402.

KOOP, C. G. & BROWAND, F. K. 1979 Instability and turbulence in a stratified fluid with shear. *J. Fluid Mech.* **93**, 135–159.

LAPRISE, R. & PELTIER, W. R. 1989 The linear stability of nonlinear mountain waves: Implications for the understanding of severe down slope wind storms. *J. Atmos. Sci.* **46**, 545–564.

LASHERAS, J. C., CHO, J. S. & MAXWORTHY, T. 1986 On the origin and evolution of streamwise vortical structures in a plane free shear-layer *J. Fluid Mech.* **172**, 231–258.

LASHERAS, J. C. & CHOI, H. 1988 Three-dimensional instability of a plane, free shear layer: an experimental study of the formation and evolution of streamwise vortices. *J. Fluid Mech.* **189**, 53–86.

LIN, S. J. & CORCOS, G. M. 1984 The mixing layer: deterministic models of a turbulent flow. Part 3. The effect of plane strain on the dynamics of streamwise vortices. *J. Fluid Mech.* **141**, 139–178.

MASLOWE, S. A. 1973 Finite amplitude Kelvin–Helmholtz billows. *Boundary-Layer Met.* **5**, 43–52.

METCALFE, R. W., ORSZAG, S. A., BRACHET, M. E., MENON, S. & RILEY, J. J. 1987 Secondary instability of a temporally growing mixing layer. *J. Fluid Mech.* **184**, 207–243.

MIKSAD, R. W. 1972 Experiments on the nonlinear stages of free-shear-layer transitions. *J. Fluid Mech.* **56**, 695–719.

NAGATA, M. & BUSSE, F. H. 1983 Three-dimensional tertiary motions in a plane shear layer. *J. Fluid Mech.* **135**, 1–26.

PATNAIK, P. C., SHERMAN, F. S. & CORCOS, G. M. 1976 A numerical simulation of Kelvin-Helmholtz waves of finite amplitude. *J. Fluid Mech.* **73**, 215–240.

PELTIER, W. R., HALLÉ, J. & CLARK, T. L. 1978 The evolution of finite amplitude Kelvin–Helmholtz billows. *Geophys. Astrophys. Fluid Dyn.* **10**, 53–87.

PIERREHUMBERT, R. T. 1986 Universal short-wave instability of two-dimensional eddies in an inviscid fluid. *Phys. Rev. Lett.* **57**, 2157–2159.

PIERREHUMBERT, R. T. & WIDNALL, S. E. 1982 The two- and three-dimensional instabilities of a spatially periodic shear layer. *J. Fluid Mech.* **114**, 59–82 (referred to herein as PW82).

STUART, J. T. 1967 On finite amplitude oscillations in laminar mixing layers. *J. Fluid Mech.* **29**, 417–440.

THORPE, S. A. 1968 A method of producing a shear flow in a stratified fluid. *J. Fluid Mech.* **32**, 693–704.

THORPE, S. A. 1971 Experiments on the instability of stratified shear flows: miscible fluids. *J. Fluid Mech.* **46**, 299–320.

THORPE, S. A. 1973 Experiments on stability and turbulence in a stratified shear flow. *J. Fluid Mech.* **61**, 731–751.

THORPE, S. A. 1985 Laboratory observations of secondary structures in Kelvin–Helmholtz billows and consequences for ocean mixing. *Geophys. Astrophys. Fluid Dyn.* **34**, 175–199.

THORPE, S. A. 1987 Transition phenomena and the development of turbulence in stratified fluids. *J. Geophys. Res.* **92**, 5231.